



TALLINN UNIVERSITY OF TECHNOLOGY

SCHOOL OF ENGINEERING

DEPARTMENT OF MATERIALS AND ENVIRONMENTAL TECHNOLOGY

**PARTIAL CATION SUBSTITUTION IN $\text{Cu}_2\text{ZnSnS}_4$
MONOGRAIN POWDERS FOR SOLAR CELL
APPLICATION**

**OSALINE KATIOONASENDUS $\text{Cu}_2\text{ZnSnS}_4$
MONOTERAPULBrites JA SELLE MÕJU PÄIKESEPATAREI
VÄLJUNDPARAMEETRITELE**

MASTER THESIS

Üliõpilane: Wisdom Chukwubuike Abazie
/nimi/

Üliõpilaskood: 184666KAYM

Juhendaja: Dr. Kristi Timmo, Senior Research Scientist
/nimi, amet/

Tallinn 2020

(On the reverse side of title page)

AUTHOR'S DECLARATION

Hereby I declare, that I have written this thesis independently.

No academic degree has been applied for based on this material. All works, major viewpoints and data of the other authors used in this thesis have been referenced.

"25" 05 2020

Author:

/signature /

Thesis is in accordance with terms and requirements

"....." 20....

Supervisor:

/signature/

Accepted for defence

"02" June 2020.

Chairman of theses defence commission:

/name and signature/

Department of Materials and Environmental Technology

THESIS TASK

Student: Wisdom Chukwubuike Abazie (name, student code)
Study programme, KAYM, Materials and Processes for Sustainable Energetics (code and title)
main speciality: Processes for Sustainable Energetics
Supervisor(s): Senior Research Scientist, Dr. Kristi Timmo, +372 620 3362 (position, name, phone)
Consultants:(name, position)
.....(company, phone, e-mail)

Thesis topic:
(in English) Partial cation substitution in Cu_2ZnSnS_4 monograin powders for solar cell application
(in Estonian) Osaline katioonasendus Cu_2ZnSnS_4 monoterapulbrites ja selle mõju päikesepatarei väljundparameetritele

Thesis main objectives:

1. To study the influence of double cation partial substitution of Cu with Ag and Zn with Cd to the Cu_2ZnSnS_4 properties by using monograin powder technology.
2. To find out the optimum initial concentration of both cations for the growth of $(Cu_{1-x}Ag_x)_{1.85}(Zn_{1-y}Cd_y)_{1.1}SnS_4$ (ACZCTS) monograin powder crystals in molten potassium iodide to achieve the highest performance of ACZCTS MGL solar cells.

Thesis tasks and time schedule:

No	Task description	Deadline
1.	Preparation of all monograin powders and characterization	05.02.2020
2.	Taking <i>J-V</i> curve measurements of the ACZCTS samples	09.03.2020
3.	Submission of thesis report	25.05.2020

Language: English **Deadline for submission of thesis:** "25" 05 2020 a

Student: Wisdom Chukwubuike Abazie "25" 05 2020 a
/signature/

Supervisor: Dr. Kristi Timmo ".....".....202... a
/signature/

Consultant: ".....".....202....a
/signature/

Head of study programme: Sergei Bereznev ".....".....202.a
/signature/

Terms of thesis closed defence and/or restricted access conditions to be formulated on the reverse side

CONTENTS

PREFACE	6
List of abbreviations and symbols.....	7
INTRODUCTION	8
1. LITERATURE REVIEW	10
1.1 Working Principle of a Solar Cell	10
1.2 Review of solar cell absorber materials.....	11
1.3 Properties of CZTS	13
1.3.1 Crystal structure	13
1.3.2 Synthesis methods of CZTS	14
1.3.3 Phase composition of CZTS.....	16
1.4 Defects in kesterites.....	18
1.5 Doping and alloying of kesterites	19
1.5.1 Ag and Cd partial substitution	22
1.6 Monograin Powder Technology.....	24
1.6.1 Overview of Monograin Powder Technology	24
1.6.2 Monograin Powder Growth.....	24
1.6.3 Monograin layer solar cells	25
1.7 Summary of literature overview and objective of the study	26
2. EXPERIMENTAL	28
2.1 Preparation of monograin powders	28
2.2 Preparation of ACZCTS monograin layer solar cells.....	30
2.3 Characterization of monograin powders	30
2.3.1 Energy-dispersive X-ray spectroscopy (EDX)	30
2.3.2 Raman Spectroscopy	31
2.3.3 Scanning electron microscope (SEM)	31
2.3.4 X-ray diffraction (XRD) analysis	31
2.4 Solar cell characteristics	32
2.4.1 Current density versus voltage (<i>I-V</i>) measurements	32
2.4.2 Quantum efficiency measurements.....	32
3. RESULTS AND DISCUSSIONS.....	33
3.1 Morphology of the monograin powders	33
3.2 Elemental composition of monograin powders (EDX)	35
3.3 Phase composition of the ACZCTS monograin powders	39

3.3.1 XRD Analysis	39
3.3.2 Raman Analysis	42
3.4 Device characterization	44
3.4.1 External Quantum Efficiency (EQE)	44
3.4.2 <i>I-V</i> curve results	46
SUMMARY	49
LIST OF REFERENCES	51

PREFACE

The thesis topic in this study was proposed by my supervisor, senior researcher Dr. Kristi Timmo. All the experimental work done with respect to this thesis was carried out in the Laboratory of Photovoltaic Materials at the Department of Materials and Environmental Technology, Tallinn University of Technology. This work was supported by the institutional research funding IUT (IUT19-28) of the Estonian Ministry of Education and Research and by the European Union through the European Regional Development Fund, Project TK141.

I would like to express my profound gratitude to my supervisor Dr. Kristi Timmo for her immense support, teachings, candor, encouragement, assistance from the very day one of this thesis to the final day. In addition, I would like to also thank other research members – Dr. Marit Kauk-Kuusik, Dr. Maris Pilvet, Dr. Jaan Raudoja, Dr. Tiit Varema and Reelika Kaupmees whose support during the experimental works were pivotal to the completion of this work. Furthermore, I am grateful for the team that assisted in the characterization measurements namely – Dr. Valdek Mikli, Dr. Arvo Mere and Dr. Mati Danilson whose support were necessary to compute the results data. Finally, I want to thank my family for their support, goodwill and prayers which kept me afloat.

In this study, two series of $(\text{Cu}_{1-x}\text{Ag}_x)_{1.85}(\text{Zn}_{1-y}\text{Cd}_y)_{1.1}\text{SnS}_4$ kesterites with varying Ag and Cd-contents were synthesized in molten potassium iodide from binary chalcogenides and elemental Sulphur by using mongorain powder growth technology. The overall aim of this study was to investigate the effects of double cation substitution of Cu and Zn respectively with Ag and Cd to the CZTS properties. The main objective was to find out the optimum initial compositional ratios of $[\text{Ag}]/([\text{Cu}]+[\text{Ag}]$ and $[\text{Cd}]/([\text{Zn}]+[\text{Cd}]$ for the growth of $(\text{Cu}_{1-x}\text{Ag}_x)_{1.85}(\text{Zn}_{1-y}\text{Cd}_y)_{1.1}\text{SnS}_4$ (ACZCTS) monograin powder crystals in molten potassium iodide to achieve the highest performance of ACZCTS MGL solar cells. The findings of this study provide that the positive effect of Ag in MGL solar cells appears only at very low concentration ratios and is detrimental to the performance at higher level. As a result, the solar cell efficiency of 8.73% was achieved by using MGL solar cells based on ACZCTS monograin powder with the initial compositional ratios of $[\text{Ag}]/([\text{Cu}]+[\text{Ag}]) = 0.01$ and $[\text{Cd}]/([\text{Zn}]+[\text{Cd}]) = 0.2$.

Key Words: kesterite, monograin powder technology, Ag substitution, Cd substitution, solar cells

List of abbreviations, symbols and their meanings

CZTSSe	Copper Zinc Tin Sulfide/Selenide
CIGS	Copper Indium Gallium Selenide Cu(In,Ga)Se_2
CdTe	Cadmium Telluride
E_g^*	Effective band gap energy
E_f	Fermi level
EDX	Energy-dispersive X-ray spectroscopy
EQE	External Quantum Efficiency
FF	Fill Factor
J_{sc}	Short-circuit current density
KI	Potassium Iodide
MGL	Monograin layer solar cell
MGP	Monograin powder
PV	Photovoltaics
PCE	Power Conversion Efficiency
QE	Quantum Efficiency
SEM	Scanning Electron Microscopy
V_{oc}	Open-circuit voltage
XRD	X-ray Diffraction

INTRODUCTION

Energy is one of the defining challenges of our time. Currently, at least 70 % of the world's energy is largely produced by fossil fuels which contributes to global warming due to carbon emissions. The advent of renewable energy technologies has given us a great hope as their incorporation can assist to reduce the dependency on fossil fuels.

Furthermore, as the world's population and industries continue to grow, this will put significant demands on our planet's limited resources including fossil fuels thus creating a high possibility of energy insecurity and even emissions. The use of Renewables doesn't only help to curb Carbon emissions but, also helps to provide dependable energy security.

Some renewable energy sources/technologies have been identified: Hydro-power, Wind, Solar, Geothermal and Biomass. These sources of renewables will play a key role in the energy of the future. This research will address the Solar energy aspect of renewable technologies.

The process of converting sunlight directly into electricity using solar cells is called photovoltaics (PV). Photovoltaics is a sustainable means of producing energy since it does not use any fossil fuel but the Sun. However, for PVs to be reliable, the constituent materials must be earth-abundant and the production technology affordable with overall minimal environmental impact. These demands gave rise to the second generation of photovoltaics, i.e., thin-film-silicon, cadmium telluride (CdTe) and copper indium gallium selenide (CIGS) where cost, raw materials availability and environmental impact were of paramount importance. Improving these three factors directly relates to the desired human empirical sustainability outcomes of security, opportunity, health from affordable, abundant clean energy, which has cross-societal, multi-regional, and transgenerational dimensions [1].

A thin film solar cell is usually identified by its absorber layer (the *p*-type semiconductor) which significantly influences the cell's properties and thus, the need to develop new absorber layers with improved properties while achieving the three measures of cost reduction, resource availability and environmental impact as described above. $\text{Cu}_2\text{ZnSnS}_4$ (CZTS) is a strong candidate for this and the aim of this study is to investigate a couple of ways its properties can be enhanced to make it a wholly dependable candidate material for thin film solar cells of the future.

Kesterites $\text{Cu}_2\text{ZnSn}(\text{S},\text{Se})_4$ (CZTSSe) are quaternary semiconductor compounds used as solar cell absorber materials. The promising features of CZTSSe is that it comprises of earth abundant and nontoxic materials, however, the power conversion efficiency of CZTSSe is still

considerably lower than CIGS and CdTe, with laboratory cell records of 11% [2] for the conventional $\text{Cu}_2\text{ZnSnS}_4$ structure, 12.6% [3] for Se-alloying kesterite based design, and 11.5% [4] have been recorded for Cd-containing $\text{Cu}_2\text{ZnSnS}_4$ solar cells. The low efficiency of these materials is mainly caused by V_{oc} deficit which is attributed to many factors, including different type of defects (point defects, vacancies, antisites) occurring within its crystal lattice, formation of secondary phases and poor synthesis methods resulting to the material not attaining the Shockley-Quisser limits of its respective solar parameters. Many methods have been proposed on how the presence of defects and secondary phases in kesterites can be reduced thus improving its solar cell properties. Among those methods is partial substitution of the individual elements in $\text{Cu}_2\text{ZnSn}(\text{S},\text{Se})_4$ with elements of same valency but different ionic radii with the aim to increase the formation energy of antisite defects. The objective of this research is to study the impact of double cation partial substitution of Cu with Ag and Zn with Cd to the $\text{Cu}_2\text{ZnSnS}_4$ properties by using monograin powder technology with the aim to increase the performance of monograin layer solar cells.

1. LITERATURE REVIEW

1.1 Working Principle of a Solar Cell

What is Photovoltaics?

Photovoltaics involve the direct conversion of light into electricity at the atomic level. There are materials known to exhibit a property known as the photoelectric effect which causes them to absorb photons of light and release electrons. When these free electrons are captured, an electric current result that can be used as electricity [5].

The diagram below (Fig 1.1) illustrates the operation of a basic photovoltaic cell, also called a solar cell. Solar cells generally comprise of a *p*-type material (holes in excess) and an *n*-type material (electrons in excess) joined to produce a *p-n* junction where an electric field is generated. When incident light energy of appropriate frequency strikes the cells, electrons are liberated and are thus captured in the form of an electric current that is electricity. This generated electricity can in turn be used to power any load such as light, tools or even saved for future use in batteries [5].

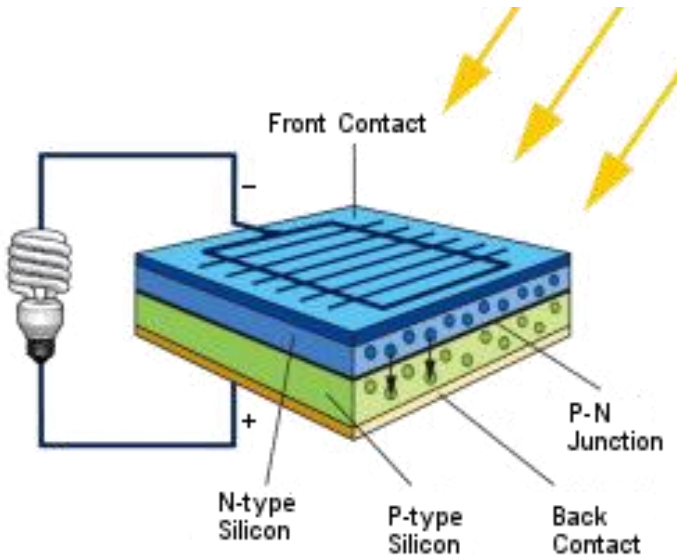


Fig 1.1 Illustration of working principle of a typical solar cell [6]

1.2 Review of solar cell absorber materials

As most of the energy in sunlight and artificial light is in the visible range of electromagnetic radiation, a solar cell absorber should be efficient in absorbing radiation at those wavelengths. Materials that strongly absorb visible radiation belong to a class of substances known as semiconductors. Semiconductors in thicknesses of about one-hundredth of a centimeter or less can absorb all incident visible light; since the junction-forming and contact layers are much thinner, the thickness of a solar cell is essentially that of the absorber. Examples of semiconductor materials employed in solar cells include silicon, gallium arsenide, indium phosphide, and copper indium selenide [7]. Thus, the main component of any solar cell device is the PV absorber material, which absorbs sunlight and transports the resulting charge carriers to electrical contacts. Currently, the most commonly used solar cell absorber is thick ($\sim 100\ \mu\text{m}$) multicrystalline silicon (Si) due to its high efficiency ($>20\%$), low cost ($<0.5\ \$/\text{W}$), and good reliability (<25 years). The closest commercial competitors for terrestrial application are CdTe and Cu(In,Ga)Se₂ (CIGS) thin-film solar cells that are as efficient yet use $\sim 100\times$ less absorber material compared to Si [8]. Aggressive development of non-silicon-based PV materials has changed the PV landscape, offering exciting near-term cost reductions for material systems like copper indium gallium selenide (CIGS) and cadmium telluride (CdTe). Quantifying material cost and the availability of these and other emerging material systems provides a critical metric to guide future research and development decisions toward a greatly expanded solar cell industry of the future [9].

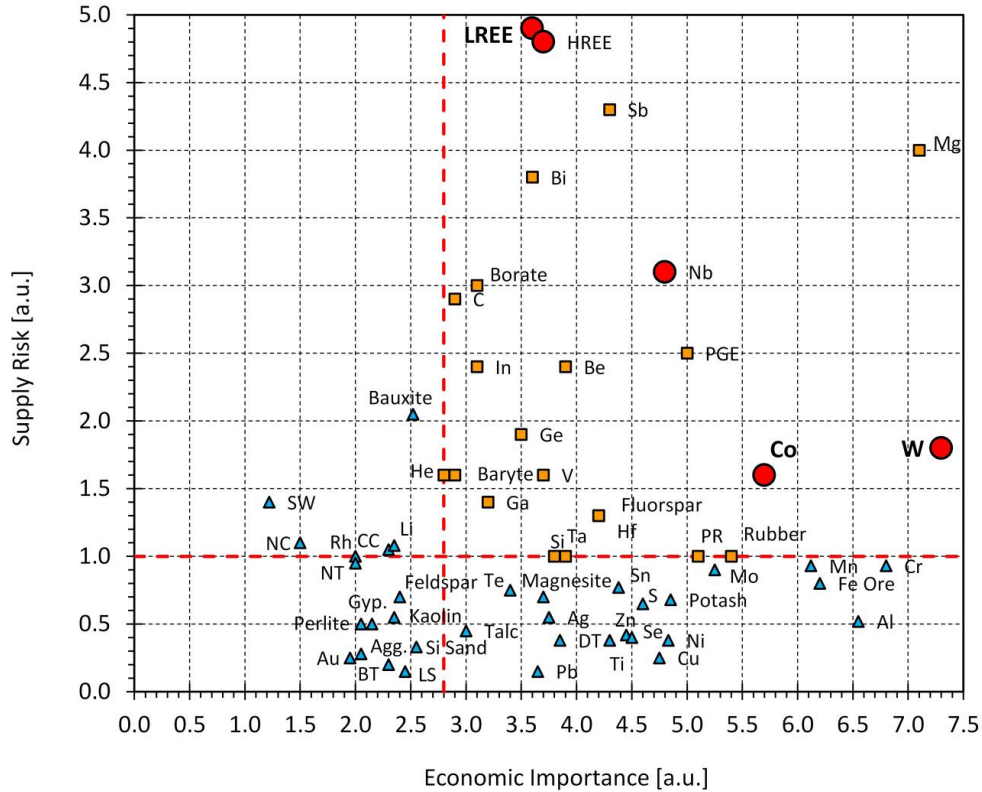


Fig. 1.2 Critical Raw Materials (CRMs) as a function of their economic importance and supply risks [10]

However, reliable and unhindered access to certain raw materials is a growing concern within the EU and across the globe. To address this challenge, the European Commission created a list of critical raw materials (CRMs) for the EU, which is subject to a regular review and update [11].

Unfortunately, Indium and Gallium which are components of CIGS and Tellurium which is a component of CdTe thin film solar cells were amongst the CRMs listed thus, creating the need to develop new CRM-free absorber materials for solar cells. This requires an upstream design and development of solutions using exclusively CRM-free technologies, together with sustainable processes based on circular economy to ensure the long-term sustainability of these new technologies. In this context, several fully inorganic PV technologies based on earth abundant elements have been identified and investigated in the past years, each of them to extent and with more or less success, aiming to figure out whether it is possible to reach a cost-efficient and competitive power conversion efficiency (PCE) fully inorganic technological solution using exclusively earth abundant elements [12] hence, due to the future requirement

of solar cells in terms of cost reduction, resource availability and environmental impact, CZTS was borne [13].

1.3 Properties of CZTS

Kesterite $\text{Cu}_2\text{ZnSnS}_4$ (CZTS) is currently the most promising absorber material emerging fully inorganic thin film photovoltaic technology based on critical raw-material-free and sustainable solutions [12]. The key property of any solar cell is its capability to absorb effectively wide spectrum of photons contained in solar radiation reaching its active surface. This feature depends on intrinsic optical and electronic properties of the semiconductor material used as the absorber layer in the cell. Absorption is described by wavelength dependent value of the absorption coefficient; the parameter being directly related to the semiconductor's energy band gap and structure [14]. $\text{Cu}_2\text{ZnSnS}_4$ has suitable photo-absorption properties, including band gap energy of 1.4 to 1.5 eV [15] and high absorption coefficient of $>10^4 \text{ cm}^{-1}$ [16] which makes it alternate potential candidate for use as *p*-type semiconductor in thin film solar cells.

1.3.1 Crystal structure

The unit cell of the quaternary semiconductor compound $\text{Cu}_2\text{ZnSnS}_4$ ($\text{I}_2\text{-II-IV-VI}_4$) is similar to the tetragonal chalcopyrite-type structure of CuInS_2 (space group $\bar{I}4_2d$). The unit cell of CZTS can be obtained from CuInS_2 by replacing In with Zn and Sn, this replacement as pointed out before, is desired in view of the limited sources and relatively high costs of In [12]. CZTS has been found in several crystal structures. Two principal tetragonal structure types are known: the kesterite (space group $\bar{I}4_2m$) and stannite (space group $\bar{I}4$) according to the varying positions of Cu and Zn in the crystal lattice as shown in the images below (Fig 1.3 left and middle) [17]. Additionally, a disordered kesterite phase has been observed, in that case copper and zinc atoms in the kesterite structure are randomly distributed (Fig 1.3 right). Fig 1.3 shows the crystal structures of the CZTS compound where the presence of the individual elements is shown at their respective co-ordinates in the crystal lattice. It can be seen that in the case of kesterite (left), Cu is present in all the corners while for stannite (middle), Zn is at the center and at the top and bottom of the crystal lattice, Sn can be seen at the top and bottom of the other two sides while S atoms are placed at the center near the Cu atoms. Presence of the atoms in the lattice crystal reflects the ratio of each element [18].

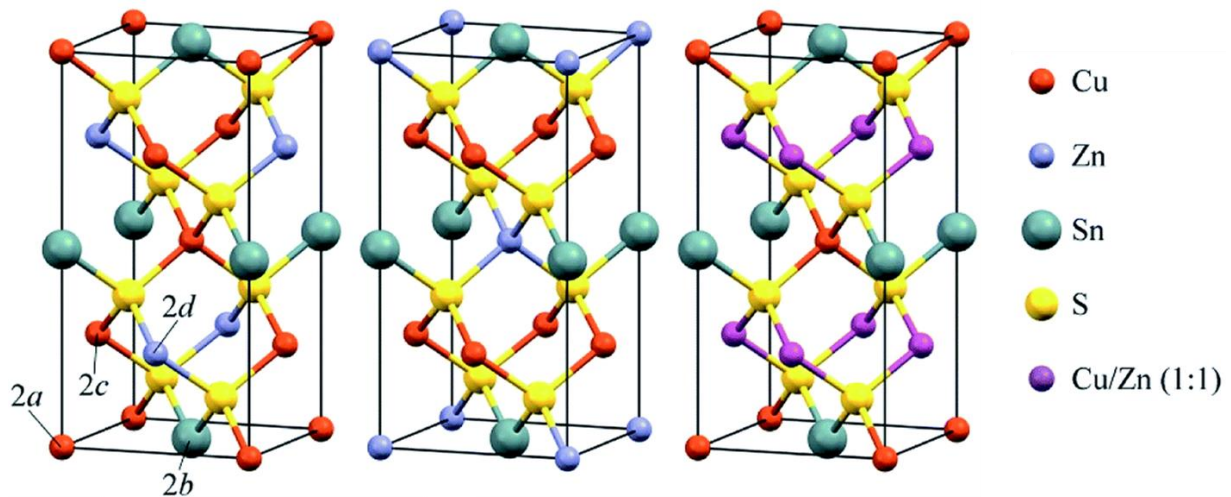


Fig 1.3 Crystal structures of $\text{Cu}_2\text{ZnSnS}_4$: kesterite (left), stannite (middle) and disordered kesterite (right) [17]

1.3.2 Synthesis methods of CZTS

The solar cell properties of CZTS materials can be improved via precise control of composition and phase purity during the synthesis. Synthesis methods of CZTS absorber material and device fabrication could be classified into solid state reaction (mainly vacuum-based) and solution-based technology.

Pulsed laser deposition (PLD) has been used to synthesize CZTS and according to the study in [19], this synthesis method generally involves the formation of the CZTS target, irradiation of laser beam on the target and annealing of the prepared films. The CZTS target is performed by solid state reaction of binary chalcogenide precursor powders: Cu_2S , ZnS and SnS_2 are mixed in the ratio of 1:1:1 followed by annealing at 750°C . A high-powered pulsed laser beam is used to evaporate the formed CZTS pellet and deposit on an already prepared substrate which could be Molybdenum or soda lime glass. Then comes the post treatment stage of the as-deposited films as in the case of most synthesis methods of CZTS including annealing and other processes to improve the crystallinity and in general, enhance the cell properties. The PLD approach offers the advantage of congruent stoichiometric transfer from the target to the films and is very suitable for multi-elements containing compounds such as the CZTS [20].

Sputtering is another common method used for preparation of CZTS thin films. It generally involves stack deposition of the precursor elements followed by sulphurization in a Sulphur-rich atmosphere to complete the formation of the CZTS compound. Different sputtering methods has been widely used to synthesize the CZTS material. In the case of modified sputtering method as described in [21], Cu/ZnS/SnS precursors were co-sputtered on Mo-coated soda lime glass using a magnetron sputtering system after which they were subjected to sulphurization. The co-sputtering process is an effective way of mixing the three target materials thoroughly at the nanoscale which promotes faster reaction during the annealing process [22]. In the single sputtering process [23], the CZTS precursors were deposited at room temperature by an RF Magnetron sputtering technique after which the resulting film was annealed in an atmosphere of H₂S and N₂.

The evaporation technique is much similar to the Sputtering technique. The major difference is that in evaporation, the particles of the target material are displaced by heat, unlike in sputtering that uses energetic particles of a plasma or gas to displace the material. There has been CZTS synthesis done by the combination of both methods as shown in the study [24] where the precursor films were firstly synthesized using elemental Cu, Zn and Sn after which they were deposited through an inductively coupled plasma assisted co-evaporation in a vacuum chamber. The CZTS films formation was finished by sulphurization through annealing in a sealed tube containing elemental Sulphur powder. In the study, the XRD analysis indicated that the plasma assisted evaporation technique could improve the properties of films crystallinity.

Other methods have also been used in synthesizing the CZTS compound such as in [25] where direct liquid coating of solution precursors was used while in [26], CZTS thin films was synthesized by single step electrodeposition technique from aqueous electrolytic bath containing 0.02 M CuSO₄, 0.01 M ZnSO₄, 0.02 M SnSO₄ and 0.02 M Na₂S₂O₃ at room temperature without stirring in a conventional three-electrode electrochemical cell assembly. In [27], the thin film was synthesized from metal chloride precursors, sulfur and oleylamine (OLA), as a ligand by a simple and low-cost hot-injection method.

Table 1.1 Progress of power conversion efficiency of CZTS-based solar cells using different deposition methods [28]

Deposition	Absorber	Institute	PCE (%)	V_{oc} (mV)	J_{sc} (mA/cm²)	E_g (eV)
Sputtering	CZTS	NNCT (Japan)	6.77	610	17.9	1.45
	CZTSSe	Stanford and AQT Solar	9.3	520	28.3	1.12
	CZTSSe	Solar Frontier (14cm ²)	10.8	502	33.5	1.2
Evaporation	CZTSe	NREL (USA)	9.15	377	37.4	1.0
	CZTSSe	IBM (USA)	8.9	385	42.6	1.15
Electrodeposition	CZTSe	IBM (USA)	7.3	567	22	8
Sol-gel	CZTS	Yonsei University (Korea)	5.1	516.9	18.9	1.5
PLD	CZTS	CNU (Korea)	4.13	700	10.01	1.54
Nanoparticle based	CZTSSe	IBM (USA)	12.6	513	35.2	1.13

In summary, there have been a very wide range of technologies and methods used for synthesizing of CZTS thin films and the technology or method used will influence the choice of precursor materials and thus, the resulting quality (crystallinity, solar cell properties, etc) of the thin films. The table below shows the highest efficiencies achieved for CZTS thin films by different groups using different synthesis methods. The world record of 12.6% PCE was reached for CZTSSe which was synthesized by hydrazine solution method [3].

1.3.3 Phase composition of CZTS

Occurrence of secondary phases is always a concern during the synthesis of CZTS. This is so because the homogeneity region for CZTS compound in phase diagram (see Figure 1.4) is only in a small range. Any slight deviation from the optimal growth conditions (input composition, temperature) will, therefore, result to the formation of unwanted secondary phases like ZnS, Cu₂SnS₃, SnS, SnS₂ and Cu₂S [29] [30] Thus, systematic control of the used synthesis method is important to provide absorber materials with homogeneous composition and good crystallinity, and finally improved solar cell properties. Fig 1.4 below shows the stringent but necessary composition and conditions that should be met for growth of kesterites [31]. It is the phase diagram of the CZTS pseudo-ternary system consisting of the binary chalcogenides: CuS, ZnS and SnS in the ratio of 50:25:25, respectively. As can be

seen in the Fig. 1.4, the CZTS phase (black dot in the image) can be exist in a very narrow range of stoichiometric ratios. Thus, implying that any deviation will result to formation of secondary phases. Regarding the ZnS and CuS (left side of the image), it can be seen that the kesterite is favored at the 55% mark which has been found to be at the $\text{Cu}/(\text{Zn}+\text{Sn}) = 0.75$ ratio, it is seen that around the 45% mark, the ratio increases to 1.25 thus implying that going upwards will result to a more Cu-rich region tending to favour the formation of secondary phase of CuS. Regarding ZnS and SnS (base side of the image), the kesterite phase was found to be stable for the Zn/Sn ratio of 0.80-1.35, a very high Zn-ratio or very poor Zn ratio will result to the kesterite losing its stability and thus lead to the formation of ZnS (for the case of high Zn/Sn ratio) or SnS (for the case of very poor Zn ratio that is high Sn ratio). Regarding CuS and SnS (right side of the image), a high content of CuS compared to the content of ZnS would lead to the formation of ternary secondary phase Cu_2SnS_3 (CTS) thus, it is quite evident that a CZTS is favoured by a Cu-poor region.

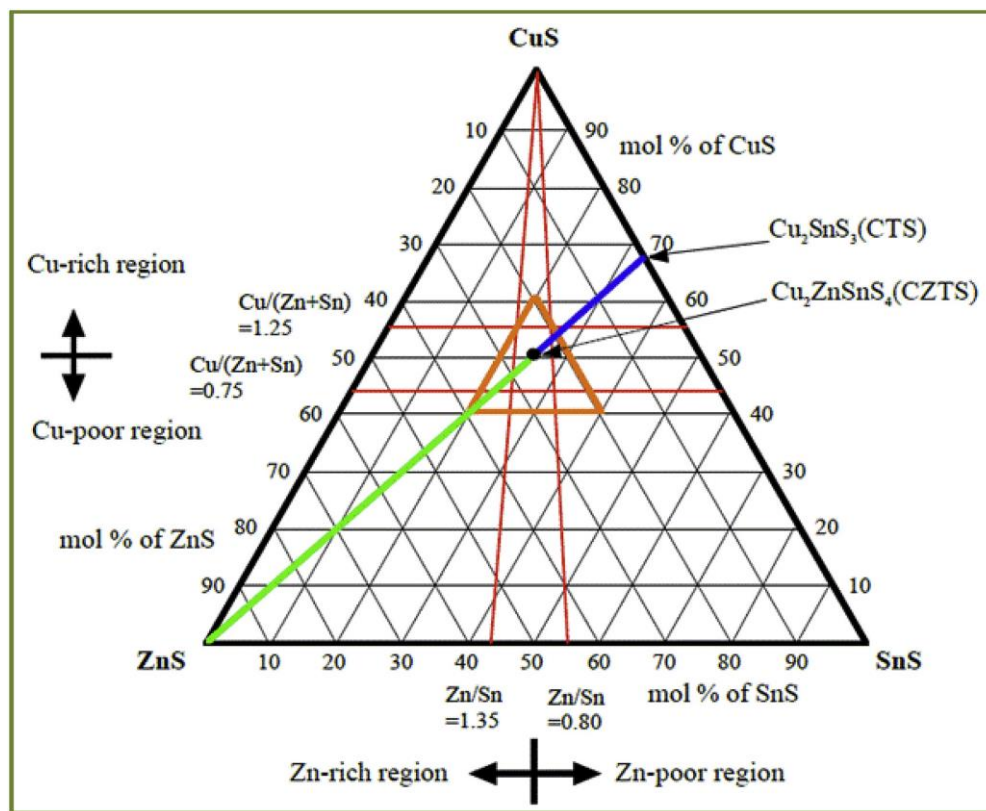


Fig 1.4 Phase diagram of the CZTS pseudo-ternary system consisting of the binary chalcogenides: CuS, ZnS, SnS in the ratio of 50:25:25, respectively [31]

1.4 Defects in CZTS

CZTS is a promising thin film material due to its composition of earth-abundant, non-toxic elements, low production costs. However, the maximum efficiency ever recorded for it or its derivative 12.6 % is quite low compared to efficiencies of other thin film solar cells such as for CIGS 23.3 % and for CdTe 22.1% [32]. Therefore, it is essential to reframe the understanding on the factors leading to this deficiency in PCE.

The presence of various deleterious defects has been the underlying cause of the poor performance of many emerging thin film solar cells including CZTS, even the record 12.6% PCE attained about 80% of the Shockley-Quisser limits for short-circuit current (I_{sc}) and Fill Factor (FF) while 59% of Shockley-Quisser limit for the open-circuit voltage (V_{oc}) [33]. The reasons for the low V_{oc} and therefore also for low PCE could be secondary phases, bulk anti-site defects, interface defects/band alignments, shorter carrier lifetimes, etc [33], [34].

Off-stoichiometry is another possible cause of poor PCE which may arise as a result of any or some of the aforementioned defects. The stoichiometric ratio of Cu, Zn, Sn and S or (Se) elements in $Cu_2ZnSn(S,Se)_4$ is 2:1:1:4, therefore under ideal conditions $Cu/(Zn+Sn) = 1$, $Zn/Sn = 1$ and $(Cu+Zn+Sn)/S = 1$. However, most of the synthesized CZTS absorber materials have $Cu/(Zn+Sn)$ ratio between 0.75 and 1, and Zn/Sn ratio between 1 and 1.25, with deviation as large as 30%. All the cells with efficiencies higher than 8% have these two ratios around 0.8 and 1.2, respectively, meaning that materials have been prepared with a Cu-poor and Zn-rich conditions.

One of the possible causes of off-stoichiometry is due to the presence of secondary phases which may be re-occurrence of some of the precursor materials used in the synthesis of the compound as mentioned in 1.3.3. For samples without secondary phases, non-stoichiometric results may be caused by a host of intrinsic defects or vacancies which may include Cu, Zn, Sn or S vacancies and their interstitial counterparts. These defects result to the aforementioned ratios deviating from unity [35]. The record maximum PCE for a Kesterite compound CZTSSe which was achieved by IBM in 2014 using the compositional ratios $Cu/(Zn+Sn) = 0.8$ and $Zn/Sn = 1.1$ with no intentional doping [36]. The most probable antisite defect is the Cu_{Zn} or Zn_{Cu} antisite defect which is as a result of low formation energy due to the similarity between the covalent radii of Cu and Zn. These samples always show a p -type behavior and when a p - n junction is formed from the p -type CZTS and n -type buffer layer, the p -type CZTS will lack effective p -to- n type inversion near the p - n junction interface due to a very high concentration of formation of Cu_{Zn} antisites at interface, this pins the Fermi

level at the middle of the band gap resulting to the deficiency in V_{oc} [37], [38]. It was found that for low Cu chemical potentials, the formation energy of the deeper Cu_{Zn} defect was found to increase whereas the formation energy of the shallower vacancy V_{Cu} was found to decrease. [37] To lower the Cu_{Zn} , Zn_{Cu} antisite related defects, Cu-poor/Zn-rich growth conditions are required to fabricate the solar cell with improved properties. However, the most-likely formation of secondary phases such as ZnS, high concentrations of Cu vacancies and off-stoichiometry will beat this purpose hence the need to develop alternative ways to remove these defects [38]. The presence of defects and impurities in chalcogenide semiconductor absorber layers as discussed above, can alter (improve or lower) the physical and electronic properties such as band gap, conductivity, photon absorption, trap level energy as well as external quantum efficiency, and open circuit potential of photovoltaic devices [39]. This will be discussed in detail in the next chapter.

1.5 Doping and alloying of kesterites

The purpose of doping and alloying of Kesterites is to improve their solar cell properties. The motivation behind doping is to improve the cell behavior by way of changing its electronic, electrical, charge transport and interface properties without altering the crystal structure and its optical properties. Alloying on the other hand implies the isoelectronic cation substitution to introduce ionic size mismatch mostly in atoms that have similar radii as will be discussed later. As can be seen from the periodic table (Fig 1.5), Group 1A metals which are the alkaline metals have been identified as candidate materials for use in doping of kesterites.

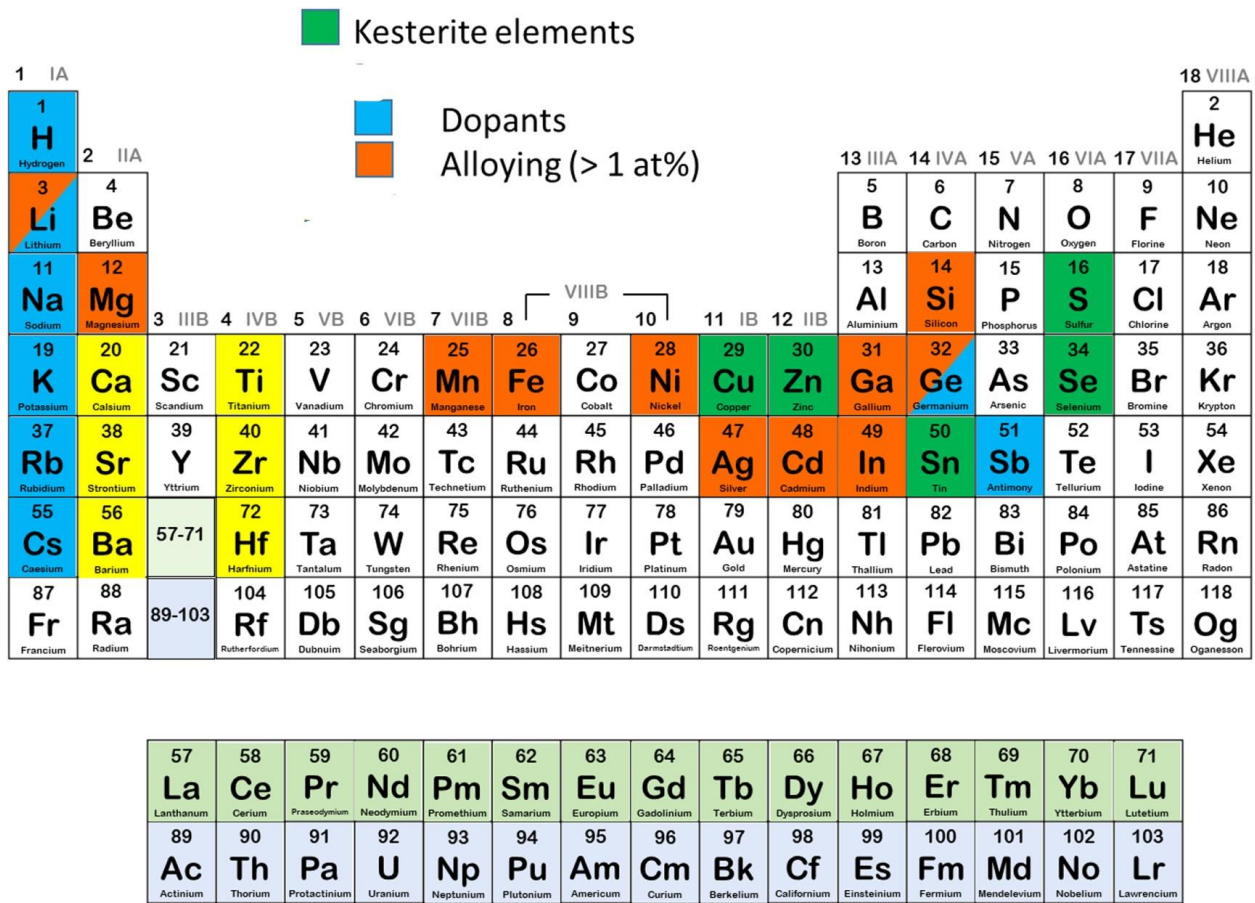


Fig 1.5 Periodic table showing some doping and alloying elements used in kesterites [36]

Alkaline doping of kesterite materials is one way to reduce the high V_{oc} deficit of solar cells by improving the cell's optoelectronic properties [40]. In [41], it was observed that Na addition to the CZTS resulted to an increase in V_{oc} and fill factor as well due to a removal of surface-near defects and an enhancement of the doping concentration. Ionic radii of Li and Cu are quite similar and thus, makes it the best candidate material among the alkali metals to be incorporated into the kesterite lattice sites to influence its properties [36]. In the investigation of the impact of different Li content in $(Li_xCu_{1-x})_2ZnSn(S,Se)_4$ ($x = 0 - 0.12$) the best PCE of 11.6% was achieved with x value of 0.06 due to the increase in carrier concentration [42]. However, the Li addition to the kesterite resulted in the decrease of V_{oc} . In the case of K, due to dissimilarity in its ionic radius resulting to a high substitution energy, it cannot form a solid solution with kesterite [43]. However, as reported in the study of the impact of K on solution processed kesterite [44], K increased the carrier density, improved carrier collection, accumulates at the CdS/CZTSSe interface thus, passivating the front interface and grain

boundaries, which resulted to the enhancement of V_{oc} and J_{sc} and hence an improvement of the PCE, it is pertinent to know that the best PCE of K-doped kesterite was found to be 7.78 % for 1.5 mol % of K. Rubidium (Rb) and Cesium (Cs) just like Potassium (K) have far larger radii than elements in kesterite and thus, this limits their doping density and in turn, will be more difficult for an increase in carrier density compared to the other lighter alkali metals however, larger atoms like Rb and Cs are favorable for the reduction of nonradiative recombination and the growth of large grains due to the relative low melting point of their binary selenides [45][36].

Comparing the five alkaline dopant metals mentioned above, it was found that the alkaline concentration resulting in highest device efficiencies is lower by an order of magnitude for the heavy alkali elements (Cs, Rb) as compared to the lighter ones (K, Na, Li) that is to say that the lighter metals required more fraction in the kesterite material than the larger elements. Furthermore, from Cs to Li, the metal ratio of nominal Sn concentration ($\text{Sn}/\text{Cu}+\text{Zn}+\text{Sn}$) required for best device properties increased from 26.5 to 33.3%, a ranking of best device performances employing alkali treatment resulted in the order of $\text{Li} > \text{Na} > \text{K} > \text{Rb} > \text{Cs}$ based on the statistics of more than 700 individual cells. A PCE of 11.5% (12.3% active area) was achieved using a “high” Li concentration with an optimized Sn content [40].

It was found in the study [46] that alloying of Mg in kesterite compound $\text{Cu}_2\text{Zn}_{1-x}\text{Mg}_x\text{Sn}(\text{S},\text{Se})_4$ ($x = 0$ to 1) maintained the kesterite phase at Mg contents up to 0.04 whereas higher Mg contents resulted to the phase separations into Cu_2SnSe_3 , MgSe_2 , MgSe and SnSe_2 . On further comparison to Mg-free samples, it was found that low content of Mg can result to an improvement in the grain growth, increase in acceptor density while causing a reduction in the number of structural defects. However, the best PCE for an Mg-alloyed kesterite material was 7.2% which is quite low compared to the PCEs of kesterite materials doped with alkali metals.

Germanium has been found to be a candidate alloy material for incorporation in kesterites. It was reported in [47] that controlled cationic atomic ratio of $\text{Ge}/(\text{Sn} + \text{Ge})$ can result to band gap grading of the kesterite material where the PCE of the $\text{Cu}_2\text{Zn}(\text{Sn}_{1-x}\text{Ge}_x)\text{Se}_4$ with the ratio of $\text{Ge}/(\text{Sn} + \text{Ge}) = 0.39$ was found to be 10.03% with an E_g of 1.19 eV and V_{oc} of 0.54 V. Further study of the impact of Ge in kesterite as presented by [48] resulted to a PCE of 12.3%, a high FF of 0.73, improved V_{oc} deficit of 0.583 V, the high FF and V_{oc} were respectively due to reduced carrier recombination at the p - n junction and band gap grading of the $\text{Ge}/(\text{Sn} + \text{Ge})$ ratio as mentioned earlier.

Manganese (Mn) offers to be a competitive alloy material for kesterite due to its isovalency with Zn, provides high cation radii mismatch compared to its fellow transition metals like Fe, Co and Ni and in addition, it is more abundant than Zn. The highest PCE as reported for Mn-alloyed CZTS materials stand at 5.7% at Mn content of 15% from Zn [49] while 8.9% for Mn content of 5% in CZTSSe [50] The improvement is attributed to the improved grain growth, better interface between absorber and buffer layers, and a change in majority defects from Cu_{Zn} to V_{Cu} [36][49][50].

1.5.1 Ag and Cd partial substitution

Owing to the defects found in kesterites resulting to a V_{oc} deficit, cation substitution has been regarded as one of the ways to alleviate defects which involves altering of the formation energy of Cu_{Zn} , Zn_{Cu} antisites and by also, altering the formation of secondary phases like ZnS that are detrimental to the performance of the solar cells [51].

In the case of substitution of Ag for Cu, as the radius of Ag^+ (1.14 Å) is much larger than that of Cu^+ (0.74 Å) and Zn^{2+} (0.74 Å), this makes it a favorable material to replace Cu. The energy of formation of Ag_{Zn} in $\text{Ag}_2\text{ZnSnS}_4$ (AZTS) is higher than the energy of formation of Cu_{Zn} in CZTS, thus, suppressing the tendency of antisite defects compared to pure CZTS [52][36][53].

Similarly, to the Ag alloying of kesterite material, the purpose of Cd alloying to the kesterites is to reduce the impact of Cu_{Zn} and Zn_{Cd} antisite defects which forms as result of the similar ionic radii of Cu and Zn where atoms of each element have high tendencies of substituting one another in the kesterite lattice. Cd^{2+} has larger ionic radii of 0.92 Å than that of Cu^+ and Zn^{2+} and thus like in the case of Ag has the capacity to increase the energy of formation of Cu_{Cd} and Cd_{Cu} antisite defects causing a reduction in the disorder and band tailing discrepancies in kesterites.

Partial double cation substitution has been found as one way of improving the performance of kesterites. In order to combine the advantages of partially substituting Cu with Ag and Zn with Cd (a double cation substitution of both elements within the crystal lattice site) is the focus of this study. The image below (Fig. 1.6) shows an illustration of the double-cation substitution of both cations of Ag and Cd for Cu and Zn, respectively.

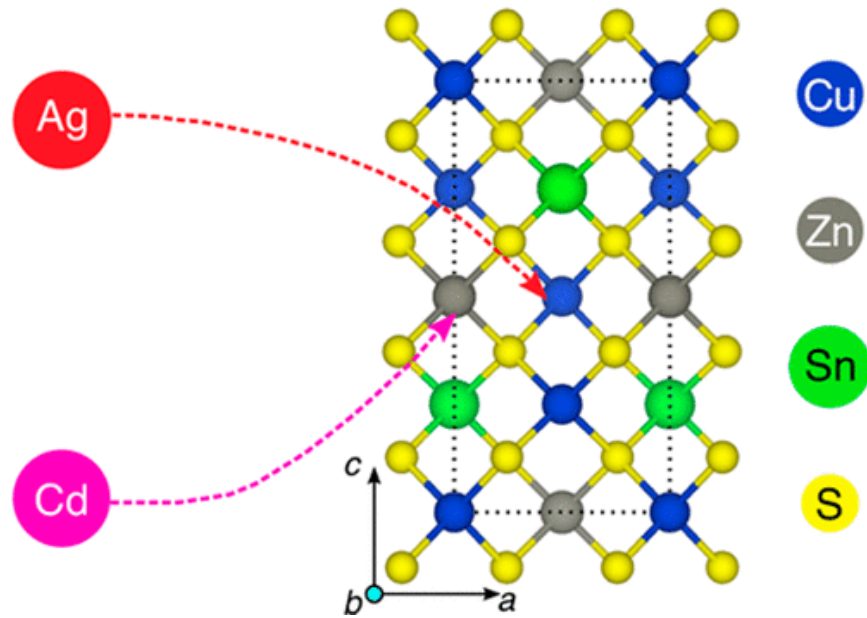


Fig. 1.6 Schematic illustration of double partial substitution of Cu and Zn respectively with Ag and Cd in CZTS lattice [54]

Regardless of the respective contents of double cation substitution, it is well understood that kesterite materials has permissible stoichiometry which when altered, will result to loss of its thermodynamic stability and deterioration of its optoelectronic property. In the case of Cu, the optimum substitution was found for $Ag/(Ag + Cu) = 0.03 - 0.10$ and in the case of Zn for $Cd/(Cd + Zn) = 0.05 - 0.40$ [51]. It was found in the study [55] that in the partial substitution of Cd for Zn in $Cu_2Zn_{1-x}Cd_xSnS_4$ ($x = 0-1.0$), the compound maintained its kesterite structure for Cd contents of the 0-0.4 range and in further addition $x > 0.6$ resulted to a change to the stannite structure. The maximum PCE of 11.5% [4] has been achieved for Zn partial substitution with Cd at the content of 40%. It was found that the controlled amounts of Zn/Cd ratio influenced the depletion width, charge density and series resistance in CZCTS materials.

In the case of partial Ag substitution, low amounts (<6% Ag) of Ag substitution is expected to suppress Cu-Zn antisite disorders though only under Cu-rich and constrained Cu-poor conditions (presence of ZnS, SnS, and Cu-deficient phases with Zn and Sn-rich conditions). Meanwhile, at a high level (>6% Ag) substitution, the Cu-Zn antisite disorder suppression is even more effective due to the higher formation energy of antisite defects [54][36]. As the maximum PCE-s for Ag doped kesterite materials have been achieved at different Ag concentrations, it indicates that the synthesis methods used can influence the overall properties of solar cells. The maximum PCE of 10.36 % being recorded for Ag content of 3%

in ACZTSSe when synthesized by solution-based method [56], similar result was also shown for the study conducted in [57] using similar synthesis method. A PCE improvement from 4.9% to 7.2% was presented by [34], where ACZTS with Ag content of 7% from Cu was synthesized by molecular solution method using metal salts precursors.

Among the potential alloying materials for kesterite solar cells, Ag and Cd has shown promising results and are widely considered the best substitutional alloying materials for Cu and Zn, respectively. As [54] pointed out, that both Cd and Ag doping have contrasting influence on the kesterite based solar cell performance through bulk stability and defect energetics, the idea is to find the optimum content of both cations which will result to a significant improvement in solar cell performance. In this study, a double cation substitution of Ag and Cd for Cu and Zn in CZTS, respectively, was performed by using monograin powder growth technology.

1.6. Monograin Powder Technology

1.6.1 Overview of the monograin powder technology

There are so many methods of synthesizing thin films solar cells as mentioned in 1.3.2 which comes with their own respective merits and demerits. However, monograin powder technology is wholly unique and differs from other thin film solar cell manufacturing methods. Monograin powder technology is advantageous as it enables the growth of $\text{Cu}_2\text{ZnSn}(\text{S},\text{Se})_4$ materials with homogeneous composition usable for monograin layer solar cells [58]. Other advantages of this technological process are that it is less costly than the common processes such as vacuum evaporation or sputtering which requires expensive production equipment. Through this synthesis method, the monograin powder formed combines: the high photoelectric parameters of monocrystals and advantages of polycrystalline materials; low cost and simple technology of materials and monograin layer (MGL) devices; possibility of making devices of a practically unlimited area and nearly 100% use of materials [59][60]

1.6.2 Monograin powder growth

Monograin powders are formed by the isothermal heating of precursor materials in the presence of liquid phase of a suitable solvent material (flux), these powders have single-crystalline grain structure with narrow-disperse granularity and found use as *p*-type semi-conductors in MGL solar cells [61].

Molten salts such of KI, CdI₂, NaI have been mainly used as flux materials for synthesis of different monograin powders [60]. Flux materials are of paramount importance during monograin powder growth process as they provide suitable medium favoring the growth of the single-grain crystals. The choice of flux material for use in powder technology will depend on a host of factors: it should be chemically stable, readily available, inexpensive and easily removable (soluble in water). A low melting temperature and low vapor pressure at the heating temperature are desirable.

Single-crystalline powders can be obtained at temperatures above the melting point of the used salt and at temperatures lower than the melting point of the semiconductor compound itself. Synthesis in molten salts enhances the rate of solid-state reactions due to the much higher diffusion rates between reaction components in the molten media, lowering the reaction temperature, increasing the homogeneity of the solid product, and controlling the particle size and shape as well as their agglomeration state. In the material formation-nucleation stage, the precursors: (1) can dissolve completely in the molten salt, with the nuclei of the product formed in the liquid phase (growth of single crystals); or (2) the initial solid particles of low-solubility precursors react with each other in the molten salt media, and the formed solid particles of the product compound start to recrystallize and grow by the mechanism of Ostwald ripening (monograin powder growth). The characteristics of monograin powder crystals are controlled by selection of the synthesis temperature, as well as the nature and amount of the salt used. The volume of the used molten salt has to exceed the volume of voids between precursor particles. In this case, the formed liquid phase is sufficient to repel both the solid precursor particles and the formed powder particles from each other and to avoid sintering caused by the contracting capillary forces arising in the solid-liquid phase boundaries. The amounts of precursors for CZTSSe and flux salt are usually taken so that the ratio of the forming volumes of solid phase V_S and liquid phase V_L is within the range 0.6–1.0 [60].

1.6.3 Monograin layer solar cells

Monograin layer solar cells are made up of unique microcrystals that form parallel connected miniature solar cells in a large module (covered with an ultra-thin buffer layer i.e the *n*-type semiconductor). Monograin layer solar cells technology provides major advantages over the conventional silicon-based solar panels – the photovoltaics cells are lightweight, flexible, can be semi-transparent, while being environmentally friendly and significantly less expensive.

A typical monograin membrane solar cell is made of monograin powder crystals with the following architecture: graphite/absorber layer/CdS buffer/i-ZnO/ZnO:Al window layer. The Figure 1.6 shows an illustration of the structure of a monograin layer solar cell. For MGL formation a monolayer of nearly uni-size CdS covered powder crystals are embedded halfway into an epoxy layer. After polymerization of epoxy, a double layer of ZnO (i-ZnO and ZnO:Al) as a window layer are deposited by radio frequency magnetron sputtering on the top of the membranes. The silver paste is used to make the front collector onto the ZnO window layer, and the structure are glued onto a glass plate. A conductive graphite paste is used for making the back contacts. A more detailed description of the preparation of MGL solar cells can be found in the Experimental part.

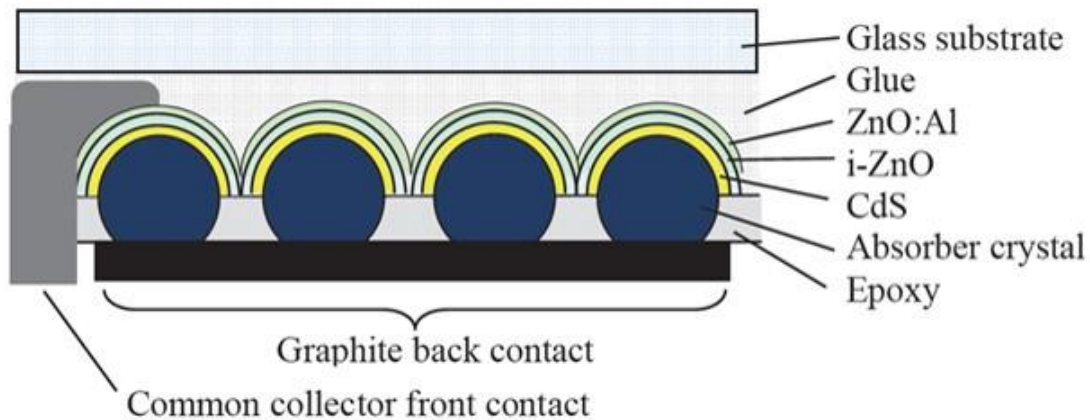


Fig. 1.7. Scheme of monograin layer solar cell [62]

1.7 Summary of literature overview and objective of the study

Renewable power capacity is set to expand by 50% between 2019 and 2024, led by solar PV [63], this expected expansion will ultimately lead to a whole new pressure on technologies and materials for solar PV. For large-scale photovoltaic application, cost-effective processes and materials are needed. Monograin layer technology combine cheap non-vacuum method for the formation of homogeneous single crystals and the possibility of using cheap, flexible, low temperature substrate production of solar cells.

The kesterite $\text{Cu}_2\text{ZnSnS}_4$ (CZTS) is attractive absorber material candidate for thin film solar cells as it offers to alleviate the material bottlenecks presented in silicon, CIGS and CdTe.

CZTS is similar to the chalcopyrite structure of CIGS but uses only earth-abundant elements. The raw materials used in CZTS are about five times cheaper than those for CIGS. To estimate of global material reserves (for Cu, Sn, Zn and S) suggest we could produce enough energy to power the world with only 0.1% of the available raw material resources. In spite of advantages that this novel material brings, the current record of the efficiency of CZTSSe and pure CZTS solar cells are 12.6% and 11%, respectively. These values are much lower than the PCE records of 23.3% for CIGS and 22.1% for CdTe [32].

In order to improve the efficiency of CZTS material, it is important to reframe our understanding on the possible causes of this deficiency and proffer ways in which these deficiencies can be reduced resulting in the improvement of solar cell performance. Cu-Zn antisite defects and formation of secondary phases have been found to be some of the factors resulting to the poor PCE. To prevent formation of these antisites, previous researches have been found that the introduction of isovalent but dissimilar atoms of ionic radii can increase the formation energies of these antisites. Ag, Cd, Mn, Fe, etc have been of interest as they all meet these requirements.

Double cation partial substitution of Cu and Zn with Ag and Cd, respectively, can be one approach to increase the energy of formation of Cu_{Zn} and Zn_{Cu} antisite defects and thus, reduce the tendency of the formation of these defects resulting to an improvement in the V_{oc} and *PCE*.

The overall aim of the current study is to investigate the impact of double cation partial substitution of Cu and Zn respectively with Ag and Cd to the CZTS properties by using monograin powder technology. The main objective is to find out the optimum initial compositional ratios of ($([\text{Ag}]/([\text{Cu}]+[\text{Ag}]))$ and ($([\text{Cd}]/([\text{Zn}]+[\text{Cd}]))$ ratio)) for the growth of $(\text{Cu}_{1-x}\text{Ag}_x)_{1.85}(\text{Zn}_{1-y}\text{Cd}_y)_{1.1}\text{SnS}_4$ (ACZCTS) monograin powder crystals in molten potassium iodide to achieve the highest performance of ACZCTS MGL solar cells. During this study, two experimental series will be prepared, in the first series one of the dopants (Cd) will be kept constant while the other one (Ag) will be varied and in the second series vice-versa.

2. EXPERIMENTAL

In this study $(\text{Cu}_{1-x}\text{Ag}_x)_{1.85}(\text{Zn}_{1-y}\text{Cd}_y)_{1.1}\text{SnS}_{4.124}$ monograin powders were prepared from binary chalcogenides in the liquid phase of a flux material KI in evacuated quartz ampoules. The synthesis-growth processes of $(\text{Cu}_{1-x}\text{Ag}_x)_{1.85}(\text{Zn}_{1-y}\text{Cd}_y)_{1.1}\text{SnS}_{4.124}$ monograin powders were performed at 740°C for 142 hours.

In [64] and [55], it was found that an addition of Cd content more than 60% from Zn in CZTS, the kesterite phase of the CZTS transforms to the stannite phase. In [37], it was found that the carrier density depreciates with increasing Ag content in CZTS and for Ag content of more than 50% from Cu the material conductivity type starts to invert from *p*-type to *n*-type. As CZTS kesterite structure needs to be maintained as well as with its carrier density, the concentration values of Cd and Ag are chosen within the limits necessary to avoid deviation or transformation to stannite structure and/or to the *n*-type material.

2.1 Preparation of monograin powders

In the first experimental series $(\text{Cu}_{1-x}\text{Ag}_x)_{1.85}(\text{Zn}_{0.8}\text{Cd}_{0.2})_{1.1}\text{SnS}_{4.124}$ monograin powders with different *x* values (*x* = 0, 0.01, 0.02, 0.03, 0.04, 0.05, 0.1 and 0.15) and constant Cd content of $[\text{Cd}]/([\text{Zn}]+[\text{Cd}]) = 0.2$ were prepared. Hereafter all *x* values are presented as atomic percentages of Ag for Cu substitution (*x* = 0, 1, 2, 3, 4, 5, 10, and 15%).

In the second experimental series $(\text{Cu}_{0.99}\text{Ag}_{0.1})_{1.85}(\text{Zn}_{1-y}\text{Cd}_y)_{1.1}\text{SnS}_{4.124}$ monograin powders with different *y* values (*y* = 0.15, 0.2, 0.25, 0.30, 0.35) and constant Ag content of $[\text{Ag}]/([\text{Cu}]+[\text{Ag}]) = 0.01$ were prepared. Hereafter all *y* values are presented as atomic percentages of Cd for Zn substitution (*y* = 15, 20, 25, 30 and 35%).

For both series the used precursor compounds CuS (3N), Ag₂S (4N) and SnS (3N) were self-synthesized in evacuated quartz ampoules by Dr. Jaan Raudoja in TalTech Laboratory, ZnS (5N) and CdS (5N) were commercially available. As the flux agent, water soluble KI (2N) was used with the volume ratio of liquid KI to solid ACZCTS compound $V_{\text{KI}}/V_{\text{ACZCTS}} (\text{cm}^3/\text{cm}^3) = 1.0$. The amount of the components for the kesterite synthesis and the amount of the flux material were taken nearly equal to provide enough volume of the liquid phase for filling the free volume between the solid particles, which is one prerequisite for monograin powder crystals growth. Before using potassium iodide powder was heated in the dynamic vacuum-

pumping process at temperatures up to 270 °C for dehydration. The binary precursors of both series were weighed in the required proportions and ratios to ensure they conform to the elemental compositions taken into account. The respective weighed precursors of both series were then mixed in a ball mill for grinding and to improve the homogeneity. The mixtures were loaded into quartz ampoules, degassed under dynamic vacuum at 100°C, sealed and heated isothermally at 740°C for about 142 hours. The growth processes were stopped by taking the samples out of the furnace and allowing them to cool naturally to room temperature. The KI flux material was completely removed using its water solubility property by leaching and rinsing with deionized water several times. The KI-free monograin powders were then dried in a hot-air thermostat and sieved into several narrow granulometric fractions between 38 and 112 µm.

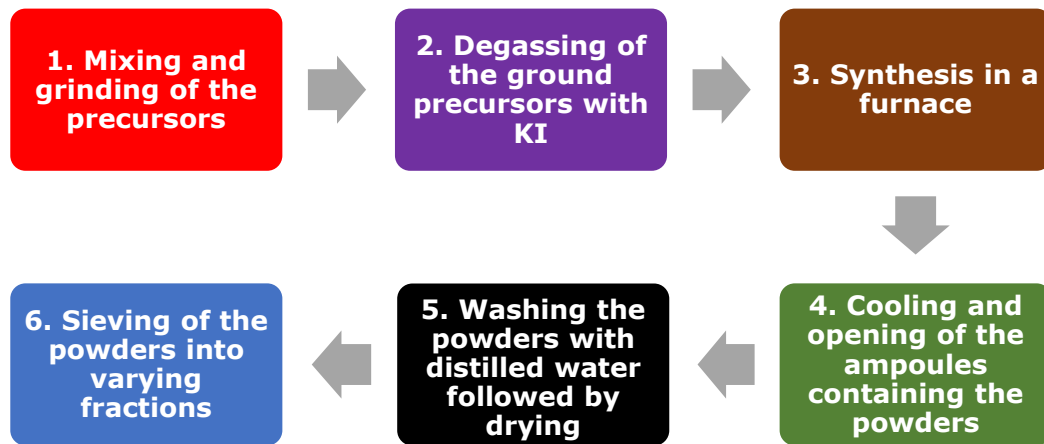


Fig. 2.1 Steps of the monograin powder growth technology from start to finish

During the synthesis-growth process at 740°C where the flux material KI ($T_M = 681 \text{ }^\circ\text{C}$) is already molten, some part of the precursors and already formed ACZCTS compound dissolve in the molten KI. This dissolved part deposits onto crystals' surfaces during cooling down period. These formations result to secondary phases and amorphous sedimentations on the powder crystals' surfaces by decreasing the perfection of crystals which will negatively affect the solar properties of the cell. Therefore, the etching of the compound is necessary to remove these precipitations. The as-grown ACZCTS monograin powders of both series were etched using combined chemical etching regime worked out for kesterite monograin powders in the TalTech Laboratory of Photovoltaic Materials (1% Br₂ in methanol solution for 10 minutes followed by etching with 10% aqueous KCN solution for 10 minutes) with the aim of removing from the crystals' surfaces the solids that precipitated from molten KI as explained above.

After the etching process, the ACZCTS samples were annealed in sealed degassed ampoules in a two-temperature-zone furnace at 840 °C in a sulfur atmosphere of 2050 Torr for 1 hour to heal the surface imperfections generated by etching and to adjust the surface composition.

2.2 Preparation of ACZCTS monograin layer solar cells

After the synthesis growth of monograin powders the CdS buffer layer was deposited on the post-treated *p*-type ACZCTS crystals through chemical bath deposition method (CBD) thereby forming the required *p-n* junction. CdS covered monograin powders were used for making the monograin layer membranes. In a membrane, the ACZCTS crystals stand independent on another and are bound together with a thin layer of epoxy. The used particle size of the absorber ACZCTS will affect the thickness of epoxy layer used which overall determines the thickness of the solar cell. After polymerization of the epoxy, the membranes were covered with an *i*-ZnO layer with a thickness of about 40–45 nm and a conductive ZnO:Al layer with a thickness of about 350–400 nm using a radio frequency magnetron sputtering system to act as a top electrode. Finally, to intensify the collection of charge carriers, conductive silver paste grid contacts were applied on top of the bilayer of the ZnO window, and the structure was glued onto a glass substrate. After removal of the supporting plastic foil from the structure, the surfaces of powder crystals at the back contact side were released partly from the epoxy by etching with concentrated H₂SO₄ for determined times. Finally, a mechanical abrasive treatment was applied to open the back contact area of crystals. Subsequently, the back contact was made with graphite conductive paste.

The prepared monograin layer solar cells have the structure of graphite/ACZCTS/CdS/*i*-ZnO/ZnO:Al/Ag/glass. In MGL solar cells every ACZCTS crystal works as an individual tiny solar cell in parallel connection. The scheme and cross-sectional view of the MGL solar cells structure is shown in Fig 1.7.

2.3 Characterization of monograin powders

2.3.1 Energy-dispersive X-ray spectroscopy (EDX)

Energy-dispersive X-ray Spectroscopy is an analytical technique employed for the chemical characterization or elemental analysis of a sample under investigation. A Bruker Esprit 1.8 EDX system (the measurement error is about 0.5 at. %) was used to investigate the elemental

composition of the monograin powders. These measurements were carried out by Dr. Valdek Mikli.

2.3.2 Raman spectroscopy

Every chemical compound or element has a wavelength which it is identifiable when incident light interacts with it. This difference in wavelength depends upon the chemical structure of the molecules responsible for causing this scattering. Raman spectroscopy is a useful tool which utilizes the results of this scattered light to gain knowledge about molecular vibrations and provide information regarding the structure, symmetry, presence of some molecules and bonding of the molecules. Raman spectroscopy permits the quantitative and qualitative analysis of the individual compounds [65]. In this study, the phase composition or presence of secondary phases were studied at room temperature by using Horiba's LabRam HR800 spectrometer equipped with a multichannel CCD detection system in the backscattering configuration using a 532 nm laser line with a spot size of 5 μm and measured within 100 seconds.

2.3.3 Scanning electron microscope (SEM)

A Scanning Electron Microscope is a powerful magnification tool that produces high-resolution three dimensional images by scanning the surface of a sample with a focused beam of electrons. The electrons that scatter off as a result of this interaction with the atoms of the sample can be analyzed with a variety of detectors that provide topographical, morphological and compositional information regarding the surface of a sample. The shape and surface morphology of the synthesized crystals were studied with a high-resolution scanning electron microscope Zeiss MERLIN. These measurements were carried out by Dr. Valdek Mikli.

2.3.4 X-ray diffraction (XRD) analysis

The powder X-ray diffraction (XRD) patterns were recorded using a Rigaku Ultima IV diffractometer with Cu K_{α} radiation ($\lambda = 1.5406 \text{ \AA}$). PDXL 2 software was used for the derivation of crystal structure information from powder XRD data. Furthermore, the XRD measurements of all samples used was carried out by Dr. Arvo Mere.

2.4 Solar cell characteristics

2.4.1 Current density versus voltage (*I-V*) measurements

Knowledge of several solar cell parameters is paramount to understanding their respective impact on the solar cell properties. Through *I-V* curve simulations, the main parameters of the solar cells were measured which are the open-circuit voltage (V_{oc}), short-circuit current density (J_{sc}), fill factor (FF) and the solar energy conversion efficiency (η).

In this study, the solar cells were characterized by measuring the *I-V* characteristics with a Keithley 2400 electrometer under standard test conditions (AM 1.5, 100 mW cm⁻²) obtained using a Newport solar simulator. The measurement error in V_{oc} values can be considered to be up to 10 mV. As the working area of the MGL solar cells is around 75% of the total area, the MGL solar cell efficiency values were re-calculated for the active area (η_{active}).

2.4.2 Quantum efficiency measurements

Quantum efficiency of a solar cell can be defined to be the ratio of the numbers of electrons in an external circuit produced by an incident photon of a given wavelength [66] thus, the effective band gap energy (E_g^*) of samples were estimated through quantum efficiency measurements. Spectral response measurements were performed in the spectral region of 350-1235 nm using a computer-controlled SPM-2 prism monochromator. The generated photocurrent was detected at 0 V bias voltage at RT by using a 250 W halogen lamp. The EQE measurements were carried out with the assistance of Dr. Mati Danilson.

3. Results and Discussions

3.1 Morphology of the monograin powders

The shape and surface morphology of the synthesized $(\text{Cu}_{1-x}\text{Ag}_x)_{1.85}(\text{Zn}_{0.8}\text{Cd}_{0.2})_{1.1}\text{SnS}_{4.12}$ and $(\text{Cu}_{0.99}\text{Ag}_{0.01})_{1.85}(\text{Zn}_{1-y}\text{Cd}_y)_{1.1}\text{SnS}_{4.12}$ monograin powder crystals were characterized by SEM. Fig 3.1 shows the SEM images of the powder crystals for the series of $(\text{Cu}_{1-x}\text{Ag}_x)_{1.85}(\text{Zn}_{0.8}\text{Cd}_{0.2})_{1.1}\text{SnS}_{4.12}$ with added Ag content ($x = 2\%$) in Fig 3.1 a-c and with the highest added Ag content ($x = 15\%$) in Fig 3.1 d-f. The powder crystals without or with low Ag content ($x = 1-5\%$) as seen also in Fig 3.1 a-c had principally tetragonal shape with rather sharp edges and smooth flat planes. The increasing of Ag content in initial powder mixture caused the formation of monograins with more rounded edges and rough crystal surfaces (Fig 3.1 d-f).

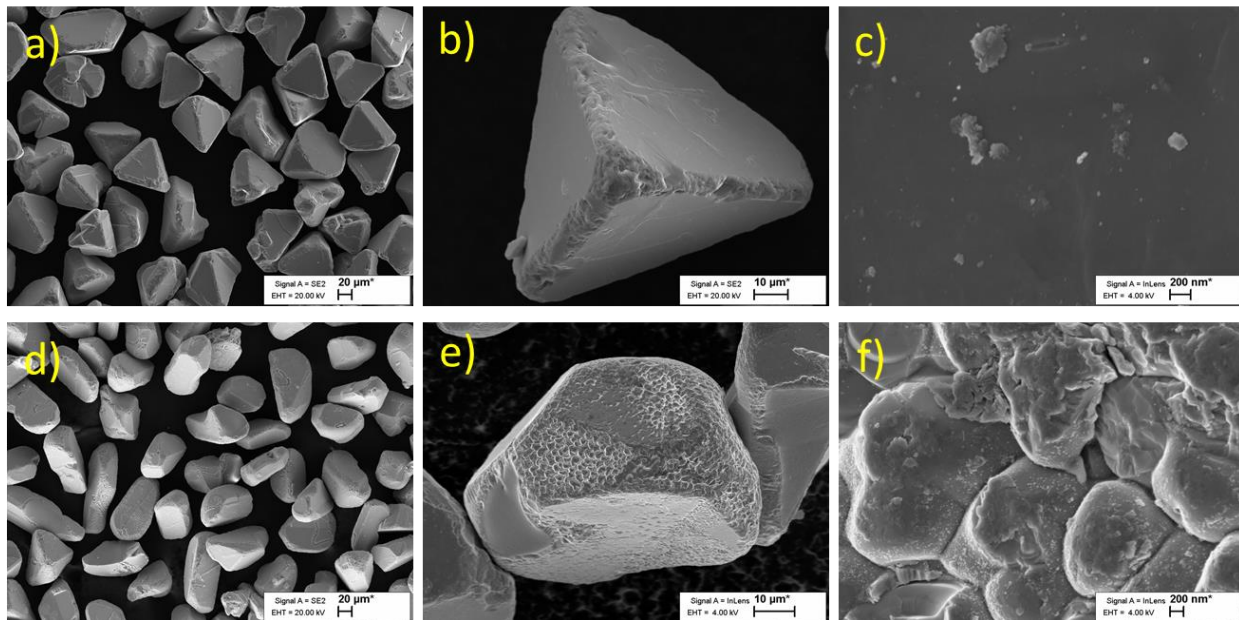


Fig. 3.1 SEM images of $(\text{Cu}_{1-x}\text{Ag}_x)_{1.85}(\text{Zn}_{0.8}\text{Cd}_{0.2})_{1.1}\text{SnS}_{4.12}$ monograin powder crystals and crystals' surfaces with $x = 2\%$ (a-c) and $x = 15\%$ (d-f).

As the synthesis growth process took place within closed ampoules under isothermal conditions, the only driving force for the monograin powder crystal growth is the difference in the surface energies of crystals with different sizes and at different places of individual crystals. During monograin crystal growth, different processes are taking place simultaneously: the dissolution of smaller crystals and the growth of bigger crystals, and the diffusion of the material through the molten phase and on the facets of crystals. When the rate of the dissolution is faster from the edges (having higher surface energies) than the

growth on planes, then more rounded crystals form. This behaviour implies that the solubility of specific compound in used flux material is high and the growth is faster as the liquid phase is richer with constituent elements. Therefore, the resulting powder becomes more rounded in shape. This means that the most-likely reason, why monograins with increasing Ag content ($x > 5\%$) had more rounded shapes than those with lower or without Ag content, is that the solubility of ACZCTS or its precursors in KI is higher than that of pure CZCTS. This also explains and could be the reason why crystals surfaces are more rough by increasing the Ag content in $(\text{Cu}_{1-x}\text{Ag}_x)_{1.85}(\text{Zn}_{0.8}\text{Cd}_{0.2})_{1.1}\text{SnS}_{4.12}$. Besides, it is known that new compounds or solid solutions of them can form in the used molten flux during the synthesis-growth process [66], [67]. During the cooling process, this part of compounds dissolved in KI at growth temperature, precipitate onto the surface of formed crystals.

Fig 3.2 shows the SEM images of the powder crystals for the series of $(\text{Cu}_{0.99}\text{Ag}_{0.01})_{1.85}(\text{Zn}_{1-y}\text{Cd}_y)_{1.1}\text{SnS}_{4.12}$ with Cd content ($y = 15\%$) in Fig 3.2 a-c and with the highest Cd content ($y = 35\%$) in Fig 3.2 d-f. It could be seen from the images that the morphology of powders crystals did not change by varying Cd content in ACZCTS from 15 to 35 %. The synthesized powder crystals had tetragonal shape with rather sharp edges and flat planes.

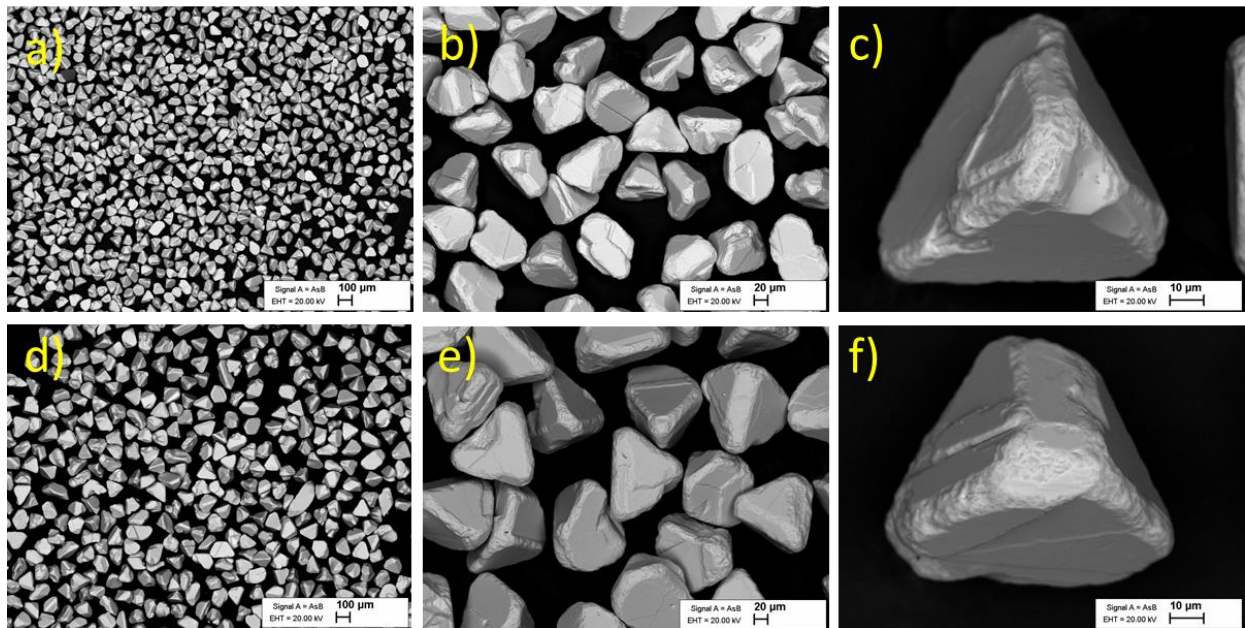


Fig. 3.2 SEM images of $(\text{Cu}_{0.99}\text{Ag}_{0.01})_{1.85}(\text{Zn}_{1-y}\text{Cd}_y)_{1.1}\text{SnS}_{4.12}$ monograin powder crystals with an input Cd content of $y = 15\%$ (a-c) and $y = 30\%$ (d-f).

3.2. Elemental composition of monograin powders (EDX)

The EDX measurement results of the average compositional ratios of synthesized $(\text{Cu}_{1-x}\text{Ag}_x)_{1.85}(\text{Zn}_{0.8}\text{Cd}_{0.2})_{1.1}\text{SnS}_{4.12}$ powder for $x = 1$ to 15% are presented in Table 3.1. This gives an overview of how the respective outcome contents of Ag and Cd varied from the input contents at the surface and at the bulk. Bulk compositional analyses were made from polished cross-section of individual crystals of ACZCTS powders as seen also in Fig. 3.4 and Fig 3.5. Compositional analysis of $(\text{Cu}_{1-x}\text{Ag}_x)_{1.85}(\text{Zn}_{0.8}\text{Cd}_{0.2})_{1.1}\text{SnS}_{4.12}$ (see Table 3.1) shows that the outcome concentration ratio of $(\text{Cu}+\text{Ag})/(\text{Zn}+\text{Cd}+\text{Sn})$ in crystals` bulk increased slightly compared to the input composition. There are no noticeable changes in the concentration ratio of $\text{Cd}/(\text{Zn}+\text{Cd})$ and $(\text{Zn}+\text{Cd})/\text{Sn}$. However, the concentration of Ag in the bulk of grown crystals is two times lower than in the surface crust for all the used x values (presented in Fig. 3.3). EDX elemental mapping of crystals (see Fig. 3.4) and line scan over the cross-section of a crystal (Fig. 3.4) shows Ag- and Cd-rich surface on the grains. At the same time Cu content on the surface is decreased compared to its constant value in the bulk of crystals. The Ag-and Cd-rich surface is most likely a result of some compounds (dissolved in KI at growth temperature) being precipitated onto the crystals` surfaces during cooling down period after synthesis-growth process. The fact that the concentration of Ag in the bulk of grown crystals (black squares in Fig. 3.3) is almost two times lower than the Ag concentration in the surface crust (blue dots) is giving a proof to the distribution of Ag between liquid (molten KI) and solid (ACZCTS) phases. Therefore, we can conclude that the Ag distribution between liquid and solid phases in the studied system is approximately equal to 2.

Table 3.1 Composition results of various Ag-alloyed $(\text{Cu}_{1-x}\text{Ag}_x)_{1.85}(\text{Zn}_{0.8}\text{Cd}_{0.2})_{1.1}\text{SnS}_{4.12}$ powders by EDX measurements (average from 8 crystals).

Input Ag content with respect to Cu (at%)	Compositional ratios of synthesized powder in bulk				Compositional ratios of synthesized powder on surface			
	$\frac{([\text{Cu}]+[\text{Ag}])}{([\text{Zn}]+[\text{Cd}]+[\text{Sn}])}$	$\frac{[\text{Ag}]}{([\text{Ag}]+[\text{Cu}])}$	$\frac{[\text{Cd}]}{([\text{Cd}]+[\text{Zn}])}$	$\frac{([\text{Zn}]+[\text{Cd}])}{[\text{Sn}]}$	$\frac{([\text{Cu}]+[\text{Ag}])}{([\text{Zn}]+[\text{Cd}]+[\text{Sn}])}$	$\frac{[\text{Ag}]}{([\text{Ag}]+[\text{Cu}])}$	$\frac{[\text{Cd}]}{([\text{Cd}]+[\text{Zn}])}$	$\frac{([\text{Zn}]+[\text{Cd}])}{[\text{Sn}]}$
0	0.92	0.00	0.19	1.08	0.92	0.00	0.21	1.07
1	0.90	0.00	0.18	1.09	0.91	0.00	0.22	1.09
2	0.89	0.00	0.19	1.09	0.88	0.01	0.23	1.06
3	0.89	0.01	0.19	1.10	0.90	0.02	0.22	1.10
4	0.89	0.01	0.19	1.10	0.89	0.03	0.21	1.10
5	0.89	0.02	0.19	1.10	0.88	0.05	0.22	1.07
10	0.89	0.05	0.19	1.10	0.88	0.09	0.21	1.07
15	0.91	0.08	0.20	1.09	0.93	0.14	0.24	1.05

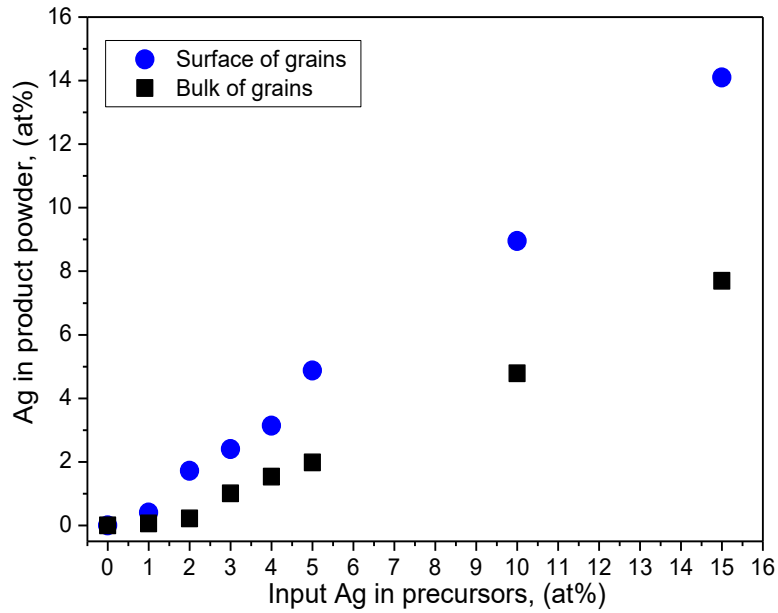


Fig. 3.3 Concentration ratios of Ag/(Cu+Ag) (at%) in the surface area (blue dots) and in the bulk (black squares) of ACZCTS monograin powder crystals in dependence of added Ag content with respect to Cu.

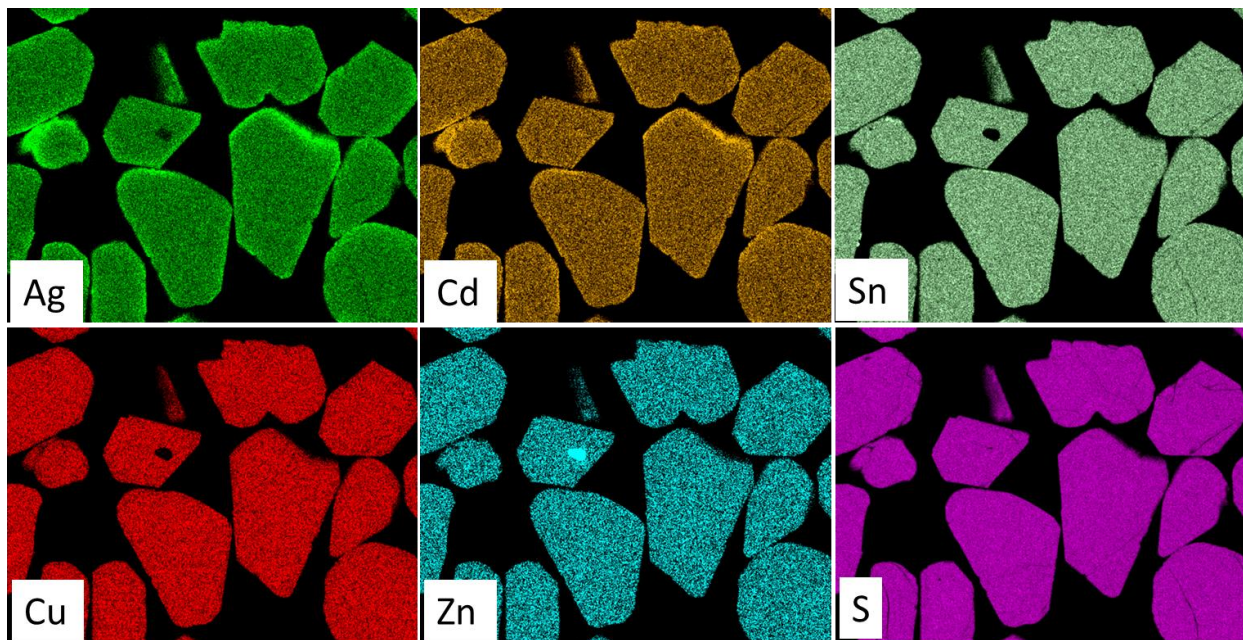


Fig. 3.4 EDX elemental mapping of Ag, Cd, Cu, Zn, Sn and S for as-grown ACZCTS polished crystals with 15% of input Ag ((ratio of $[Ag]/([Cu]+[Ag]) = 0.15$))

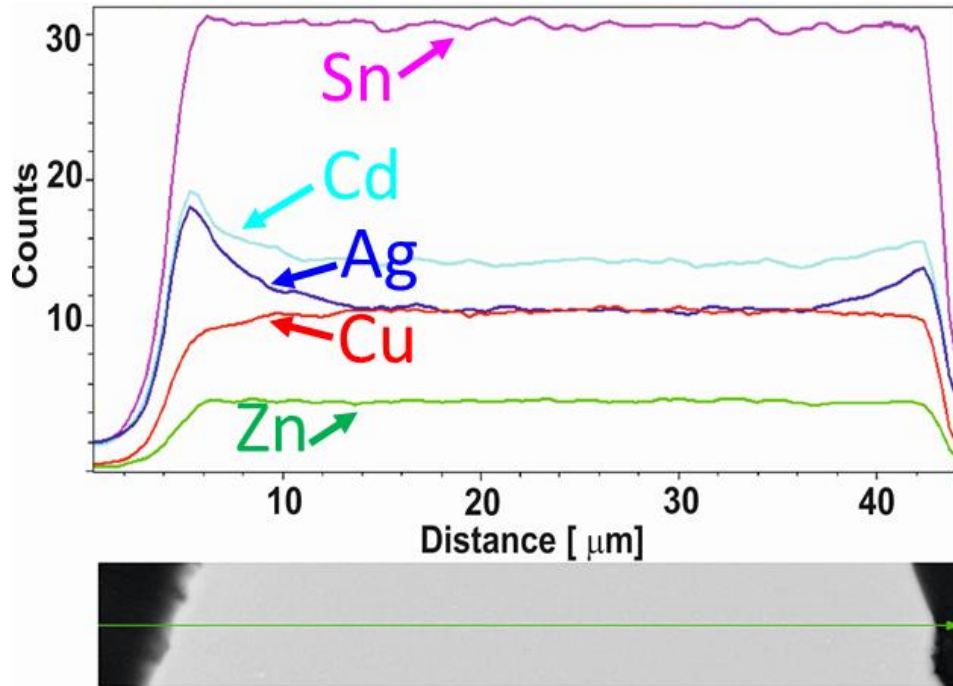


Fig. 3.5 EDX line scan over cross-section of a crystal of the as-grown ACZCTS polished crystals with 15% of input Ag

In order to investigate the influence of Zn substitution by Cd to the synthesized powder bulk composition, the EDX analysis was also performed from polished $(\text{Cu}_{0.99}\text{Ag}_{0.01})_{1.85}(\text{Zn}_{1-y}\text{Cd}_y)_{1.1}\text{SnS}_{4.12}$ powder crystals. Table 3.2 presents the EDX measurement results of the average compositional ratios of synthesized ACZCTS powders with Cd content of 15 to 35%. It can be seen from the results that the ratio of $[\text{Cd}]/([\text{Zn}]+[\text{Cd}])$ in synthesized powders is close to the input ratio in precursors.

Table 3.2 Composition results of various Cd-alloyed $(\text{Cu}_{0.99}\text{Ag}_{0.01})_{1.85}(\text{Zn}_{1-y}\text{Cd}_y)_{1.1}\text{SnS}_{4.12}$ powders by EDX measurements (average from 8 crystals).

Input Cd content with respect to Zn (at%)	Compositional ratios of synthesized powder in bulk				Compositional ratios of synthesized powder on surface			
	$\frac{([\text{Cu}]+[\text{Ag}])}{([\text{Zn}]+[\text{Cd}]+[\text{Sn}])}$	$\frac{[\text{Ag}]}{([\text{Ag}]+[\text{Cu}])}$	$\frac{[\text{Cd}]}{([\text{Cd}]+[\text{Zn}])}$	$\frac{([\text{Zn}]+[\text{Cd}])}{[\text{Sn}]}$	$\frac{([\text{Cu}]+[\text{Ag}])}{([\text{Zn}]+[\text{Cd}]+[\text{Sn}])}$	$\frac{[\text{Ag}]}{([\text{Ag}]+[\text{Cu}])}$	$\frac{[\text{Cd}]}{([\text{Cd}]+[\text{Zn}])}$	$\frac{([\text{Zn}]+[\text{Cd}])}{[\text{Sn}]}$
15	0.90	0.00	0.13	1.09	0.90	0.00	0.17	1.10
20	0.90	0.00	0.18	1.09	0.91	0.00	0.22	1.09
25	0.92	0.00	0.23	1.08	not analyzed			
30	0.91	0.00	0.28	1.09	0.88	0.00	0.32	1.07
35	0.93	0.00	0.32	1.05	0.91	0.01	0.40	1.05

Figure 3.6 shows the EDX elemental mapping of crystals and Figure 3.7 the line scan over the cross-section of a crystal for the $(\text{Cu}_{0.99}\text{Ag}_{0.01})_{1.85}(\text{Zn}_{1-y}\text{Cd}_y)_{1.1}\text{SnS}_{4.12}$ powder with Cd content $y = 35\%$. EDX elemental mapping shows uniform distribution of all elements over polished crystals without significantly higher concentration on the crystals' surfaces. Slightly higher concentration of Cd and Ag is seen in the line scan in Figure 3.7, but the thickness of this Cd- and Ag-rich layer is very low compared with the Ag varied series.

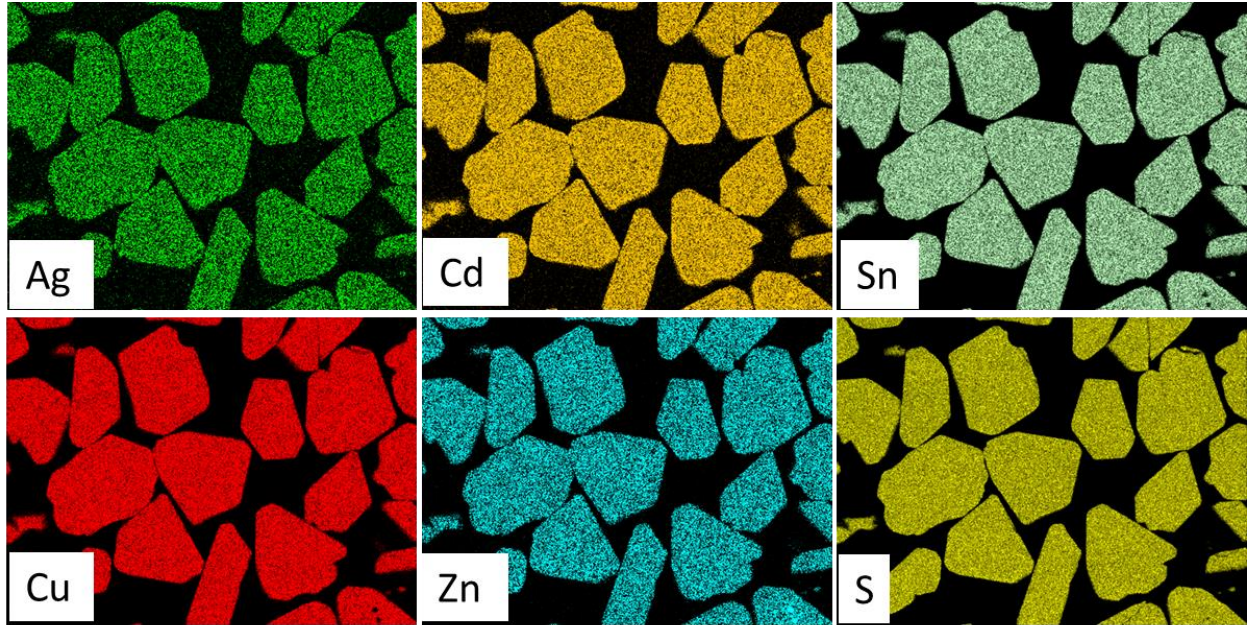


Fig. 3.6 EDX elemental mapping of Ag, Cd, Cu, Zn, Sn and S for as-grown ACZCTS polished crystals with 35% of input Cd ((ratio of $[\text{Cd}]/([\text{Zn}]+[\text{Cd}]) = 0.35$))

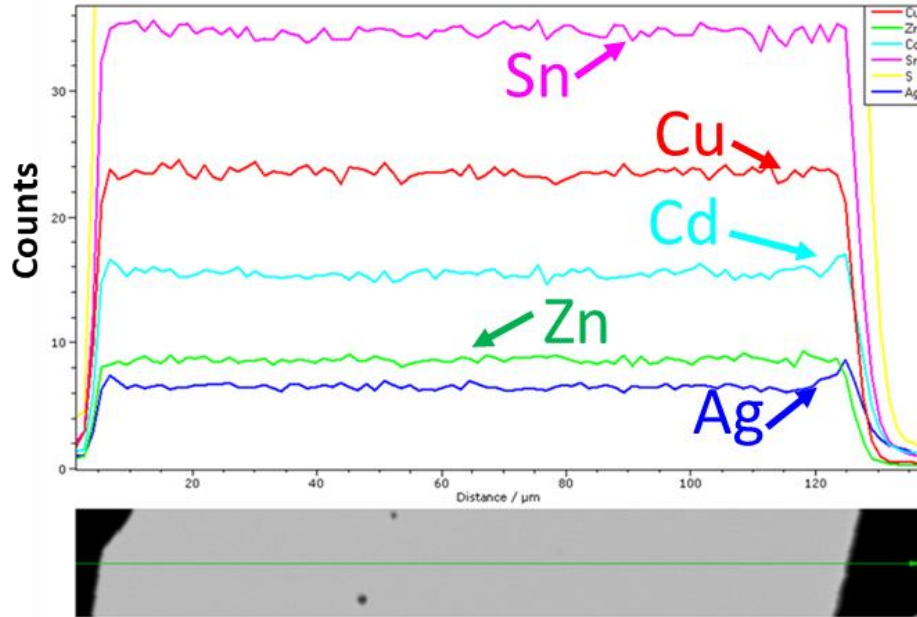


Fig. 3.7 EDX line scan over cross-section of a crystal of the as-grown ACZCTS polished crystals with 35% of input Cd

From the EDX mapping and line scan results we can conclude that the Ag and Cd rich layer on the crystals` surfaces and the thickness of it is related to the Ag concentration in the input material composition (seen in Fig. 3.4 and Fig. 3.5) and is not in dependence of Cd concentration in ACZCTS (Fig. 3.6 and Fig. 3.7).

3.3. Phase composition of the ACZCTS monograin powders

3.3.1 XRD Analysis

XRD patterns of the increasing Ag content in the Ag-varied series are as shown in Fig 3.8a. All the diffraction peaks including the major peaks (112), (200), (220), (312) and (224) could be indexed according to a tetragonal kesterite-type phase (ICDD PDF-2 Release 2019 RDB, 01-085-7033) with different Ag content. No secondary phases were detected. Lattice expansion from higher angles to lower angles was observed with increasing Ag content. Fig 3.8b shows the enlarged view of the (112) plane shift from 28.28 to 28.12 ° which is in agreement with previously reported data for Ag alloyed kesterite. The X-ray diffraction patterns were used to calculate values of the lattice parameters (*a* and *c*) for all powders used by Rietveld refinement as shown in Fig 3.9. A linear increase of the lattice parameter values

(*a* and *c*) was observed upon replacement of Cu with Ag, as the ionic radius of Ag^+ (1.14 Å) is larger than that of Cu^+ (0.74 Å). The obtained values are in good agreement with the results reported in the literature for Ag substituted kesterites and suggest that Ag is incorporated in the CZCTS lattice [68]–[70].

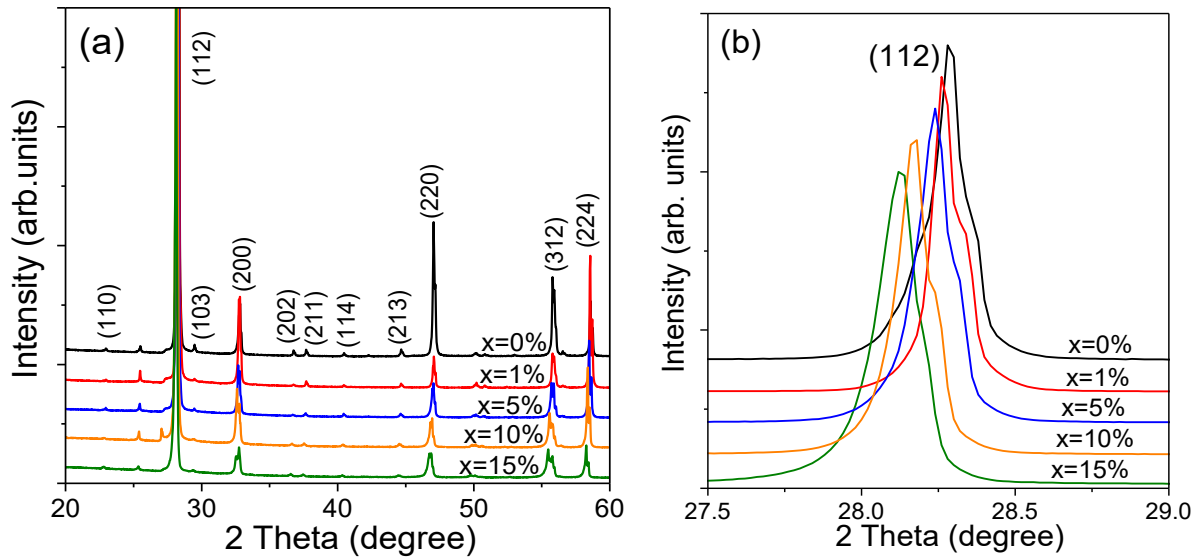


Fig. 3.8 (a) X-ray diffraction patterns of the Ag-varied ACZCTS series, (b) the enlarged view of the (112) diffraction peaks.

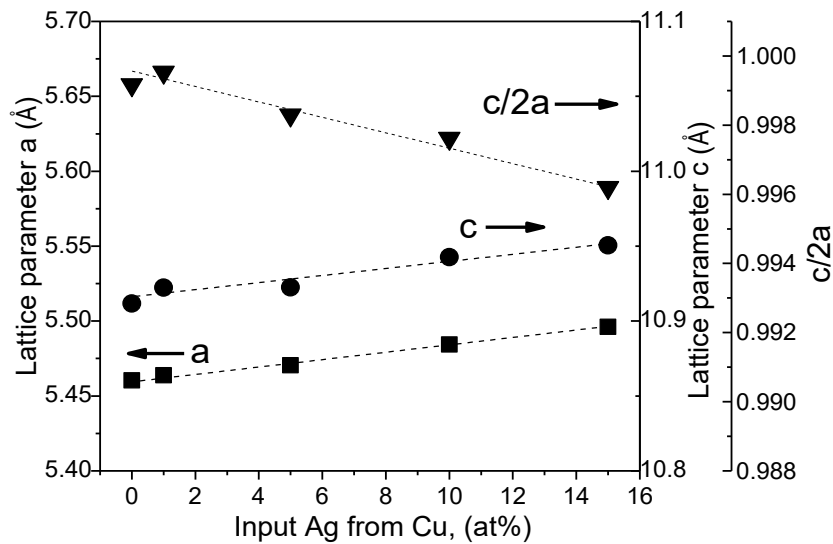


Fig. 3.9 Lattice parameters of *a*, *c*, and *c*/*2a* as a function of the Ag content in $(\text{Cu}_{1-x}\text{Ag}_x)_{1.85}(\text{Zn}_{0.8}\text{Cd}_{0.2})_{1.1}\text{SnS}_{4.12}$.

Figure 3.10 shows the XRD patterns of Cd varied $(\text{Cu}_{0.99}\text{Ag}_{0.01})_{1.85}(\text{Zn}_{1-y}\text{Cd}_y)_{1.1}\text{SnS}_{4.12}$ monograin powders. All the diffraction peaks could be indexed according to a tetragonal kesterite-type phase (ICDD PDF-2 Release 2019 RDB, 01-082-9163) with different Cd contents. No secondary phases were detected. Fig 3.10b shows the enlarged view of the (112) diffraction peaks. The peaks shifted to the lower angle side with an increase in Cd content in the MGP-s. In Fig. 3.11 are presented lattice constants for the powders with different Cd content. The a -axis constant increases linearly as the Cd content increases from 15 to 35%. The shift in (112) XRD peak from 28.39 to 28.28 ° and expansion of the lattice can be attribute to the replacement of smaller Zn^{2+} (0.74 Å) with larger Cd^{2+} (0.95 Å) in the kesterite lattice and is evident that Cd is incorporated in the ACZCTS lattice.

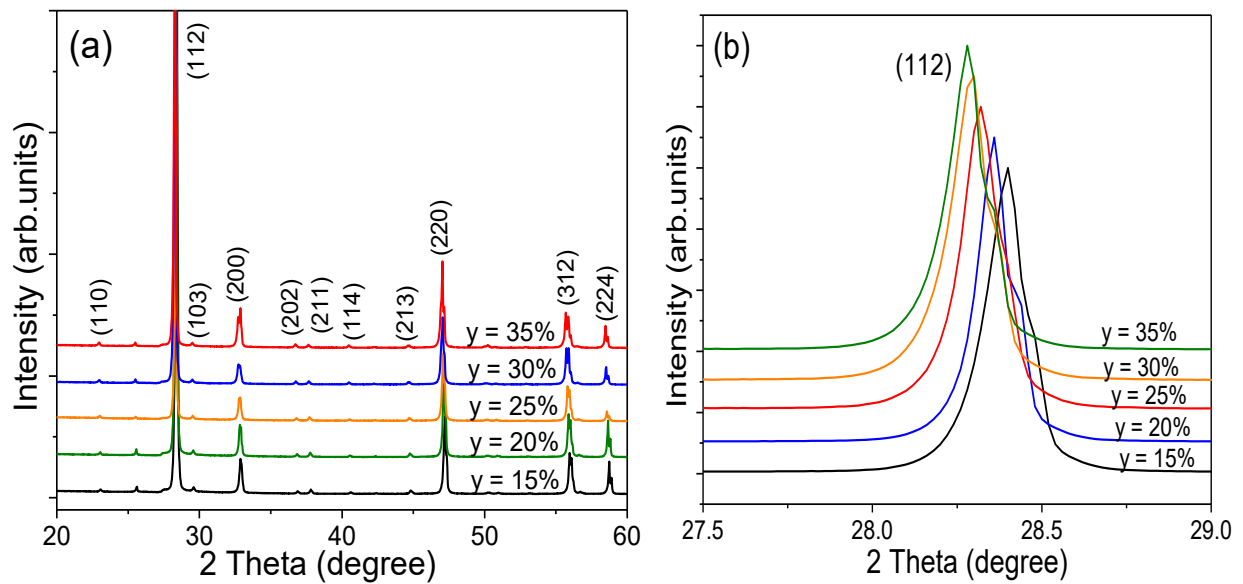


Fig. 3.10 (a) X-ray diffraction patterns of the Cd-varied ACZCTS series, (b) the enlarged view of the (112) diffraction peaks

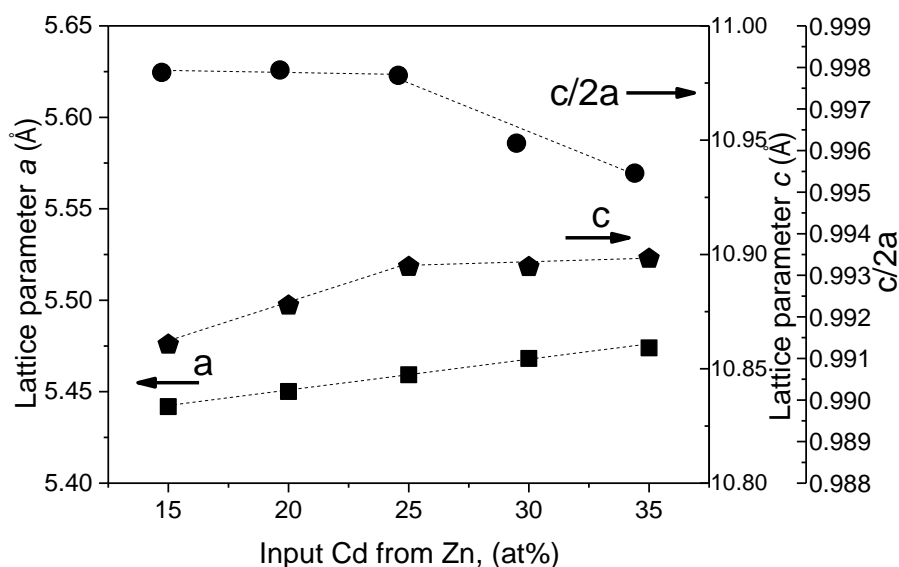


Fig. 3.11 Lattice parameters of a , c , and $c/2a$ as a function of the Cd content in $(\text{Cu}_{0.99}\text{Ag}_{0.01})_{1.85}(\text{Zn}_{1-y}\text{Cd}_y)_{1.1}\text{SnS}_{4.12}$

3.3.2 Raman Analysis

Raman spectroscopy measurements of both series were carried out to investigate the unwanted coexisting secondary phases that cannot be distinguished by XRD in ACZCTS due to the similar XRD patterns of $\text{Zn}(\text{Cd})\text{S}$, Cu_2SnS_3 and $\text{Cu}_2\text{ZnSnS}_4$ and in addition, to confirm the partial substitution of the cation.

The Raman spectra of the Ag-varied samples (for $x = 0 - 15\%$) are shown in Fig. 3.12a and their corresponding A1 peaks are shown in Fig. 3.12b. The Raman spectra of CZCTS powder crystals exhibited an intense peak of 336 cm^{-1} and three weak peaks at 287 , 362 and 372 cm^{-1} which all correspond to kesterite phase and are in conformity with results observed in other papers [71], [72]. As can be seen in Fig. 3.12b, the spectra showed the shift in A1 peak (from $336 - 333\text{ cm}^{-1}$) which reflects on increasing Ag content.

The Raman spectra of the Cd-varied monograin powders are shown in Fig. 3.13a with peak of 337 cm^{-1} and three weak peaks at 286 , 362 and 372 cm^{-1} which all correspond to kesterite phase and are in conformity with results observed in other papers. As can be seen in Fig. 3.13b, the spectra showed the shift in A1 peak (from 337 to 332.7 cm^{-1}) which corresponds to increasing Cd content in powders ($y = 15 - 35\%$). The shift of Raman scattering peak at 337 cm^{-1} to the lower wavenumber side by increasing the Cd content in ACZCTS could be attributed also to the increase in the crystal lattice parameters caused by the substitution of

Zn⁺ with bigger Cd⁺. Similar behavior was observed when Cu⁺ were partially substituted with heavier and bigger Ag⁺ [73].

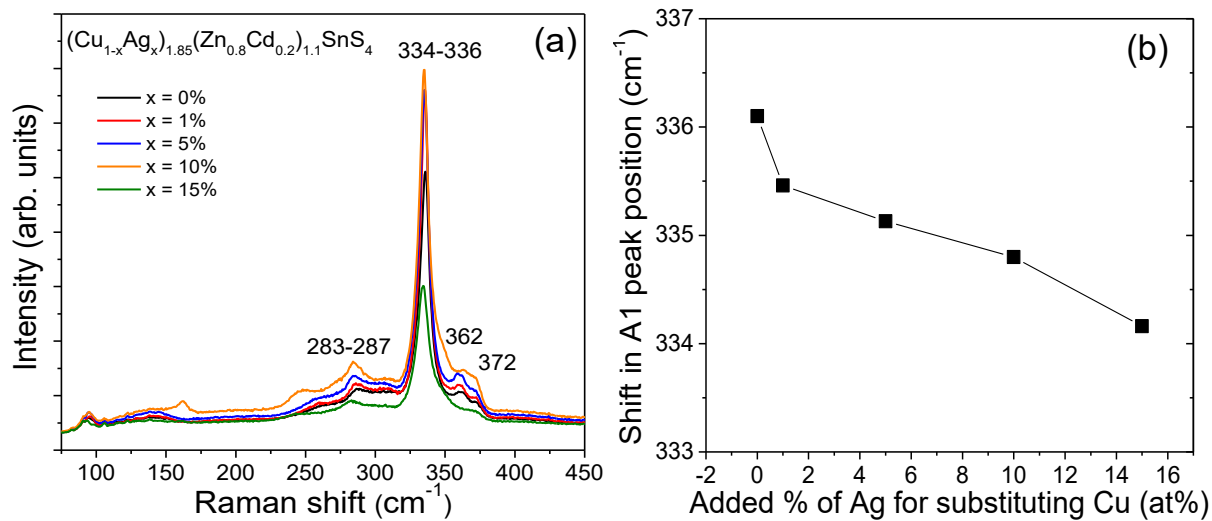


Fig. 3.12 a) Raman measurements of ACZTS series for Ag contents ($x = 0-15\%$). b) A1 peak mode vs Ag content in $(\text{Cu}_{1-x}\text{Ag}_x)_{1.85}(\text{Zn}_{0.8}\text{Cd}_{0.2})_{1.1}\text{SnS}_{4.12}$.

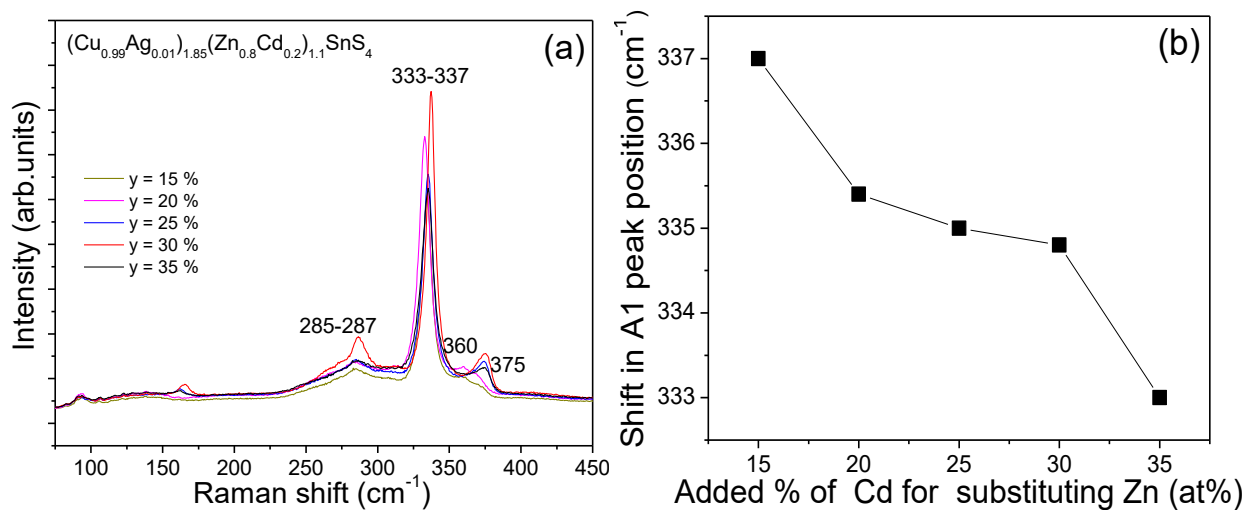


Fig. 3.13 a) Raman measurements of ACZTS series for Cd contents ($y = 15-35\%$). b) A1 peak mode vs Cd content in $(\text{Cu}_{0.99}\text{Ag}_{0.01})_{1.85}(\text{Zn}_{1-y}\text{Cd}_y)_{1.1}\text{SnS}_{4.12}$

3.4 Device characterization

3.4.1 External Quantum Efficiency (EQE)

Both series of the Ag-varied and Cu-varied monograin powders were used as absorber materials (*p*-type) in MGL solar cells. Prior to that, the as-grown samples had to undergo post-treatment where they were chemically etched and later annealed in a sulphur atmosphere, this process was done in order to improve the crystallinity of the powders, remove secondary phases and to generally improve the solar cell properties. External quantum efficiency (EQE) analysis was used to estimate the effective bandgap energy (E_g^*) of the absorber materials as the evaluation of E_g^* from the optical absorption or reflectance spectra of the monograin powders is challenging. The EQE of samples of both series was measured as a function of the incident light wavelength at room temperature. The normalized EQE spectra of monograin powder solar cells based on $(\text{Cu}_{1-x}\text{Ag}_x)_{1.85}(\text{Zn}_{1-y}\text{Cd}_y)_{1.1}\text{SnS}_{4.12}$ for $x = 0-15\%$ and for $y = 15 - 35\%$ are presented in Figure 3.14 and Figure 3.15, respectively. The E_g^* can be evaluated by constructing an $(\text{EQE})^2$ vs E curves [74] from the linear segment of the low energy side. The inset graph of Fig. 3.14 shows how the Ag content in the absorber material influences the effective band gap energy values. A slight increase of the E_g^* from 1.503 eV to 1.528 eV when increasing the Ag content in ACZCTS monograin powder materials was observed as seen in the graph. It is pertinent to know that the Ag content of 15% had the maximum E_g^* achieved and furthermore, the range of band gap was similar to the band gap values for pure (without Ag and Cd) kesterites (1.4 to 1.5 eV). The inset graph of Fig 3.15 shows how the varied Cd contents in the Cd-varied series influenced the effective band gap energy values of the ACZCTS monograin powder materials. The linear decrease of E_g^* from 1.535 to 1.445 eV with increasing Cd content in ACZCTS was observed.

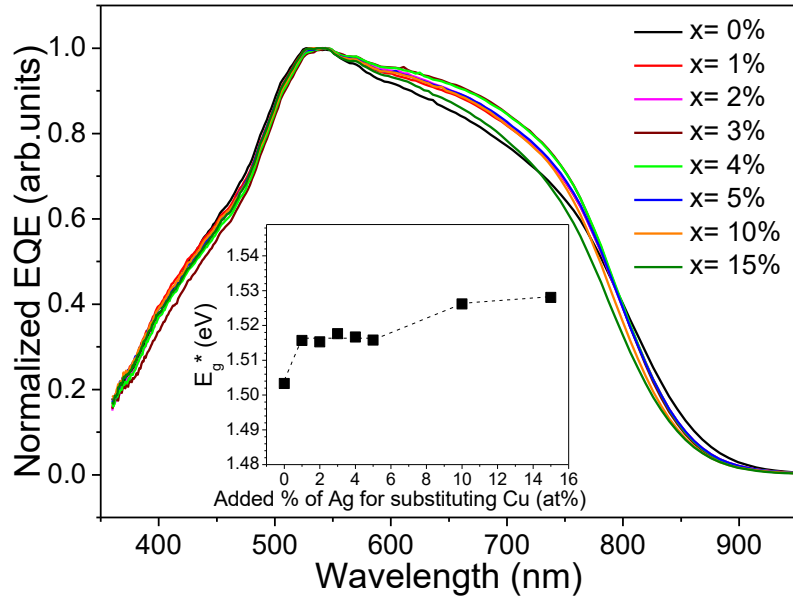


Fig.3.14 Normalized external quantum efficiency spectra of $(\text{Cu}_{1-x}\text{Ag}_x)_{1.85}(\text{Zn}_{0.8}\text{Cd}_{0.2})_{1.1}\text{SnS}_{4.12}$ MGL solar cells with an input Ag content of 0 to 15%. The inset graph shows the influence of Ag content on the effective band gap energy (E_g^*) values

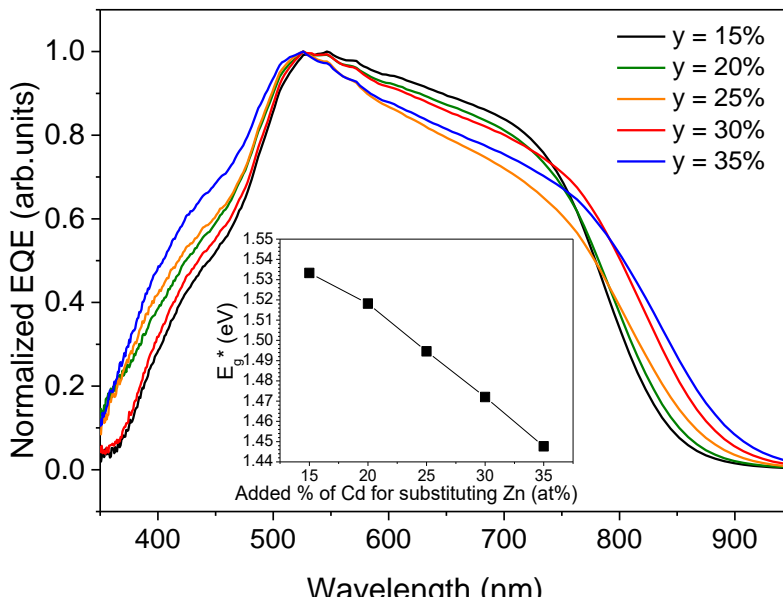


Fig.3.15 Normalized external quantum efficiency spectra of $(\text{Cu}_{0.99}\text{Ag}_{0.01})_{1.85}(\text{Zn}_{1-y}\text{Cd}_y)_{1.1}\text{SnS}_{4.12}$ MGL solar cells with an input Cd content varied from 15 to 35%. The inset graph presents the effective band gap energy (E_g^*) values depending on the input Cd content.

3.4.2 I-V curve results

Further investigations were carried out in order to determine the influence of the cation partial substitution of Ag and Cd to the MGL solar cell performance. *I-V* characteristics of both series was accomplished using a Newport solar simulator as earlier mentioned in 2.4.1. Fig. 3.16 and Table 3.3 show the respective influence of different Ag content ($x = 0, 1, 3, 4, 5, 10$ and 15%) in MGP to the solar cell parameters: short circuit current density (J_{sc}), open circuit voltage (V_{oc}), fill factor (FF), and the efficiency (PCE). We can see how the Ag influenced the parameters of the cell, on addition of Ag, the solar cell's PCE increased from 6.62% ($x = 0$) to maximum of 8.73% ($x = 1\%$) but further addition of Ag kept the PCE around 8.0% at Ag content of $x = 10\%$. For a higher content at 15% of Ag from Cu, the PCE dropped to 7.09% due to the decrease in V_{oc} despite the continuous increase in the bandgap energy values. The V_{oc} and J_{sc} had similar trend as the PCE though there was no noticeable change in the FF . The increase of V_{oc} on addition of Ag was probably due to the increase in the formation energy of Cu_{Zn} and Zn_{Cu} antisites defects which was responsible for the poor V_{oc} on undoped kesterites [73] as mentioned in 1.5.1.

In Fig. 3.17 and Table 3.4 are seen the influence of the varied Cd contents to the solar cell parameters. We can see that on increase of Cd content from 15% to 20%, there was a notable slight increment in the J_{sc} and FF at 20% though a decline in the V_{oc} , the overall result was that the efficiency increased slightly at this content. However, further addition of Cd ($y = 25\%$) resulted to a decline in all the solar cell parameters. Further increase in Cd content in ACZCTS ($y = 30$ and 35%) resulted to an increase in the PCE and slight decline afterwards. The reduction of V_{oc} on increasing Cd content agreed with results found in [73] where it was concluded that at high values of Cd, the formation of antisite defects ceases thus resulting to a diminishing value of the V_{oc} and efficiency. Although, the solar cells based on MGP with Cd content of 20 % had slightly better efficiency than the solar cells with Cd content of 15% due to its higher values of the FF and J_{sc} which compensated the loss in V_{oc} .

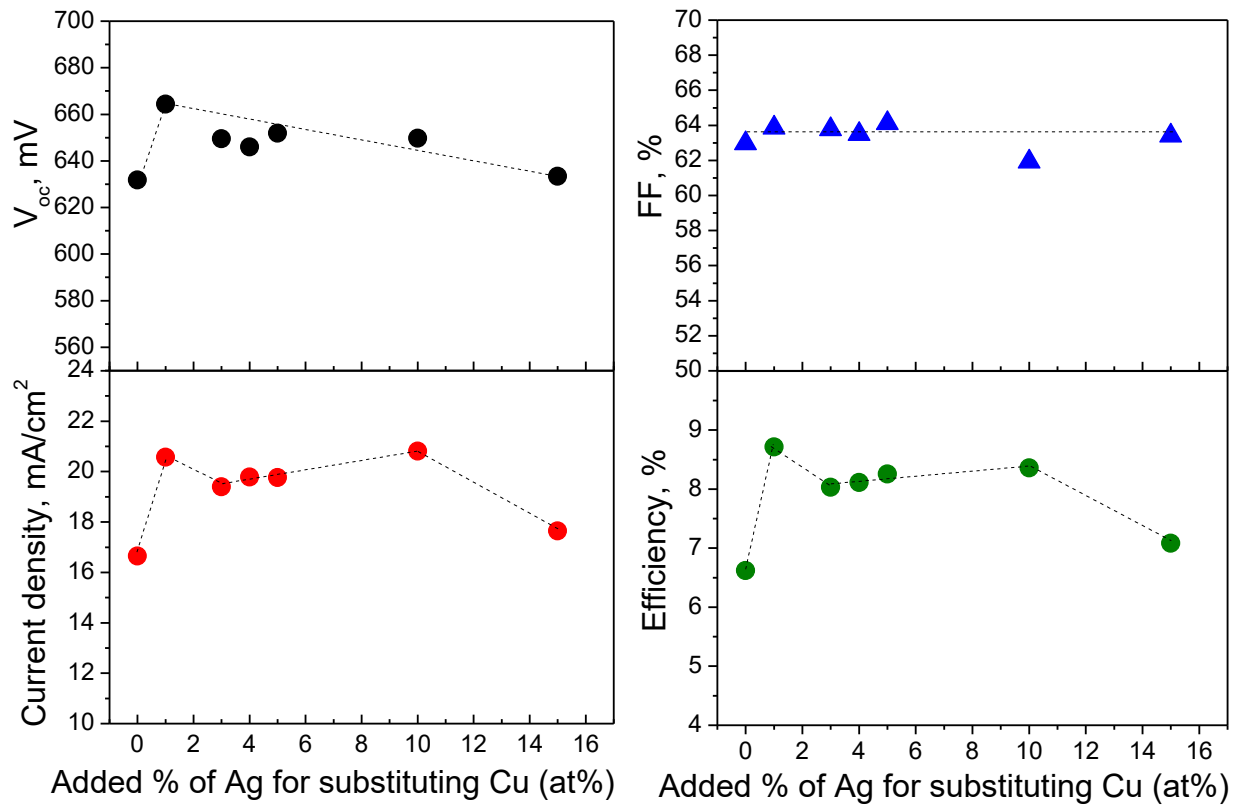


Fig 3.16 The I - V curve parameters (J_{sc} , V_{oc} , FF and PCE) of the Ag-varied ($x = 0 - 15\%$) ($Cu_{1-x}Ag_x$)_{1.85}(Zn_{0.8}Cd_{0.2})_{1.1}SnS_{4.12} MGL solar cells.

Table 3.3 below shows the summary of the solar cell parameters of the best Ag-varied cells including the effective band gap energy values.

Input Ag content with respect to Cu (%)	FF (%)	J_{sc} (mA/cm ²)	V_{oc} (mV)	PCE (active area)	E_g^* (eV)
0	62.96	18.73	632	6.62	1.503
1	63.86	20.57	664	8.73	1.515
3	63.77	16.41	649	8.04	1.517
4	63.50	18.04	646	8.12	1.516
5	64.11	19.76	652	8.26	1.516
10	61.92	20.81	650	8.37	1.526
15	63.41	17.64	633	7.09	1.528

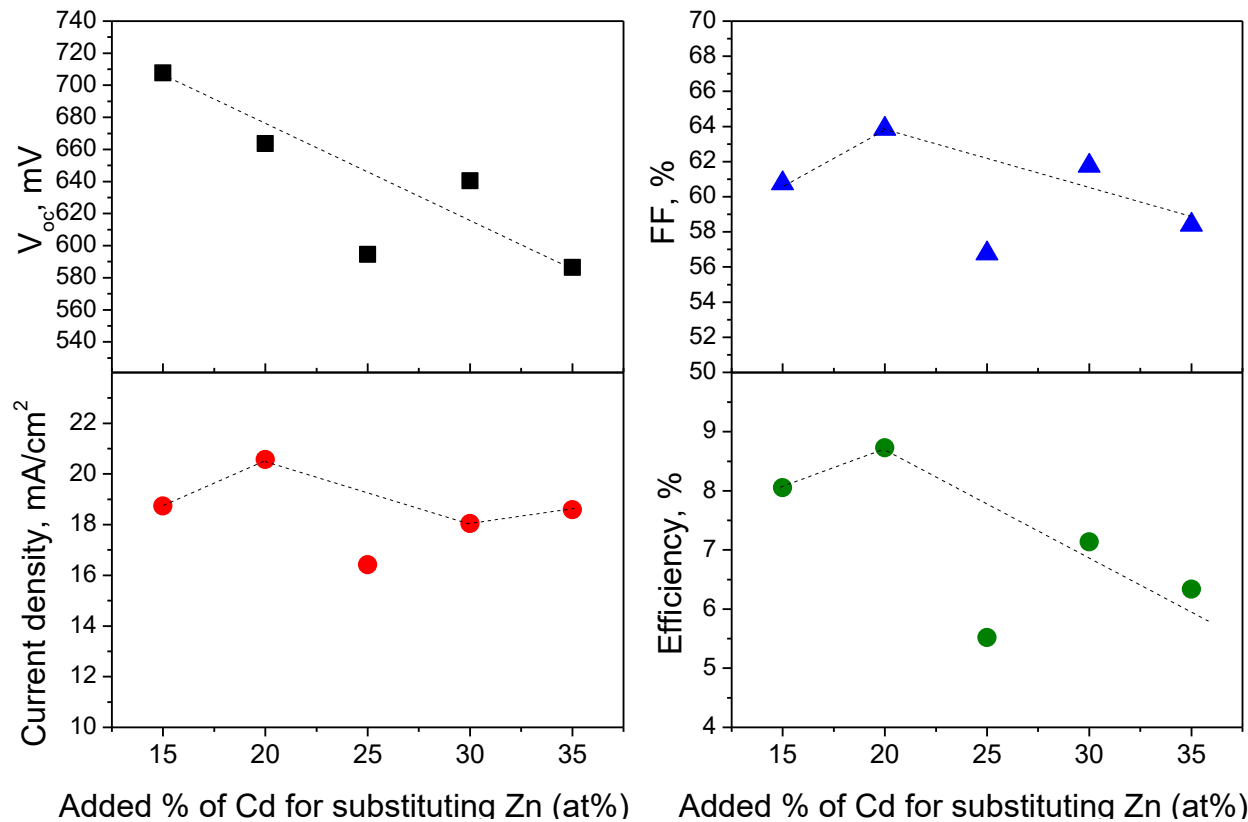


Fig. 3.17 The I - V curve parameters (J_{sc} , V_{oc} , FF and PCE) of the Cd-varied ($y = 15 - 35\%$) ($Cu_{0.99}Ag_{0.01}$)_{1.85}(Zn_{1-y}Cd_y)_{1.1}SnS_{4.12} MGL solar cells.

Table 3.4 below shows the summary of the solar cell parameters of the best Cd-varied cells including the effective band gap energy values.

Input Cd content with respect to Zn (%)	FF (%)	J_{sc} (mA/cm ²)	V_{oc} (mV)	PCE (active area)	E_g^* (eV)
15	60.75	18.73	707.63	8.05	1.535
20	63.86	20.57	663.71	8.73	1.519
25	56.77	16.41	594.55	5.52	1.499
30	61.76	18.04	640.52	7.14	1.470
35	58.39	18.59	586.39	6.34	1.445

SUMMARY

The objective of this master thesis was to prepare solid solutions of $(\text{Cu}_{1-x}\text{Ag}_x)_{1.85}(\text{Zn}_{1-y}\text{Cd}_y)_{1.1}\text{SnS}_4$ (ACZCTS) in the form of monograin powders with the aim to study the impact of double cation partial substitution of Cu with Ag and Zn with Cd to the $\text{Cu}_2\text{ZnSnS}_4$ properties and to the monograin layer (MGL) solar cell parameters.

In this study, $(\text{Cu}_{1-x}\text{Ag}_x)_{1.85}(\text{Zn}_{1-y}\text{Cd}_y)_{1.1}\text{SnS}_{4.124}$ monograin powders were synthesized from binary chalcogenides in the liquid phase of KI as the flux material in evacuated quartz ampoules at 740°C for 142 hours. Two experimental series were prepared: in the first series Cd was kept constant ($y = 20\%$) while Ag was varied ($x = 0 - 15\%$) and in the second series Ag was kept constant ($x = 1\%$) and Cd was varied ($y = 15 - 35\%$).

It was found that $(\text{Cu}_{1-x}\text{Ag}_x)_{1.85}(\text{Zn}_{1-y}\text{Cd}_y)_{1.1}\text{SnS}_4$ monograin powders with different ratios of $[\text{Ag}]/([\text{Cu}]+[\text{Ag}])$ and $[\text{Cd}]/([\text{Zn}]+[\text{Cd}])$ can be synthesized in the liquid phase of KI and used as absorber materials in MGL solar cells.

- EDX analysis of the as-grown materials in the entire first series revealed that the Ag concentration was not equal in the precursor's mixture and in the synthesized materials showing different distribution between liquid and solid phases. The Ag distribution between liquid and solid phases in the studied system was found to be approximately equal to 2. By varying Cd content in the monograin powders, it was found that the ratio of $[\text{Cd}]/([\text{Zn}]+[\text{Cd}])$ in synthesized powders was close to the input ratio in precursors.
- SEM micrographs showed that by increasing the input Ag content in precursor mixtures resulted in the formation of monograins with more rounded edges and rough crystal surfaces. The morphology of monograins did not change by varying Cd content in ACZCTS.
- XRD analyses confirmed the Ag and Cd incorporation in the ACZCTS lattice. Lattice expansion from higher diffraction angles to lower angles was observed with increasing Ag or Cd content in $(\text{Cu}_{1-x}\text{Ag}_x)_{1.85}(\text{Zn}_{1-y}\text{Cd}_y)_{1.1}\text{SnS}_4$.
- The Raman spectra of the Ag-varied monograin powders showed a shift in A1 peak from 336 to 334 cm^{-1} which corresponds to increasing Ag content in powders ($x = 0 - 15\%$) and is caused by the substitution of Cu^+ with bigger Ag^+ . Similar behavior was observed when Zn^+ were partially substituted with heavier and bigger Cd^+ .
- The effective band gap energy values showed slight increase from 1.503 eV to 1.528 eV with the raising Ag content in $(\text{Cu}_{1-x}\text{Ag}_x)_{1.85}(\text{Zn}_{0.8}\text{Cd}_{0.2})_{1.1}\text{SnS}_4$. The substitution of Zn with Cd in the ACZCTS decreased linearly E_g^* values from 1.535 to 1.445 eV.

- The best solar cell efficiency of 8.73% was achieved with MGL solar cell based on $(\text{Cu}_{1-x}\text{Ag}_x)_{1.85}(\text{Zn}_{1-y}\text{Cd}_y)_{1.1}\text{SnS}_4$ monograin powder with Ag content of $x = 1\%$ and Cd content of $y = 20\%$.

LIST OF REFERENCES

- [1] V. Fthenakis, "Sustainability of photovoltaics: The case for thin-film solar cells," *Renewable and Sustainable Energy Reviews*, vol. 13, no. 9, pp. 2746–2750, Dec-2009, doi: 10.1016/j.rser.2009.05.001.
- [2] C. Yan *et al.*, "Cu₂ZnSnS₄ solar cells with over 10% power conversion efficiency enabled by heterojunction heat treatment," *Nature Energy*, vol. 3, no. 9, pp. 764–772, Sep. 2018, doi: 10.1038/s41560-018-0206-0.
- [3] W. Wang *et al.*, "Device Characteristics of CZTSSe Thin-Film Solar Cells with 12.6% Efficiency," *Advanced Energy Materials*, vol. 4, no. 7, p. 1301465, May 2014, doi: 10.1002/aenm.201301465.
- [4] C. Yan *et al.*, "Beyond 11% Efficient Sulfide Kesterite Cu₂Zn_xCd_{1-x}SnS₄ Solar Cell: Effects of Cadmium Alloying," *ACS Energy Letters*, vol. 2, no. 4, pp. 930–936, Apr. 2017, doi: 10.1021/acseenergylett.7b00129.
- [5] "How do Photovoltaics Work? | Science Mission Directorate." [Online]. Available: <https://science.nasa.gov/science-news/science-at-nasa/2002/solarcells>. [Accessed: 18-Feb-2020].
- [6] "How do Solar Panels Work | The Renewable Energy Hub." [Online]. Available: <https://www.renewableenergyhub.co.uk/main/solar-panels/how-solar-panels-work/>. [Accessed: 29-Apr-2020].
- [7] "Electric circuit | Britannica.com." [Online]. Available: <https://www.britannica.com/technology/electric-circuit>. [Accessed: 18-Feb-2020].
- [8] A. Zakutayev, "Brief review of emerging photovoltaic absorbers," *Current Opinion in Green and Sustainable Chemistry*, vol. 4, Elsevier B.V., pp. 8–15, 01-Apr-2017, doi: 10.1016/j.cogsc.2017.01.002.
- [9] C. Wadia, A. P. Alivisatos, and D. M. Kammen, "Materials availability expands the opportunity for large-scale photovoltaics deployment," *Environmental Science and Technology*, vol. 43, no. 6, pp. 2072–2077, Mar. 2009, doi: 10.1021/es8019534.
- [10] A. H. Tkaczyk, A. Bartl, A. Amato, V. Lapkovskis, and M. Petranikova, "Sustainability evaluation of essential critical raw materials: cobalt, niobium, tungsten and rare earth elements," *Journal of Physics D: Applied Physics*, vol. 51, no. 20, p. 203001, Apr. 2018, doi: 10.1088/1361-6463/AABA99.
- [11] "Critical raw materials | Internal Market, Industry, Entrepreneurship and SMEs." [Online]. Available: https://ec.europa.eu/growth/sectors/raw-materials/specific-interest/critical_en. [Accessed: 14-Feb-2020].
- [12] S. Giraldo, Z. Jehl, M. Placidi, V. Izquierdo-Roca, A. Pérez-Rodríguez, and E. Saucedo, "Progress and Perspectives of Thin Film Kesterite Photovoltaic Technology: A Critical Review," *Advanced Materials*, vol. 31, no. 16, p. 1806692, Apr. 2019, doi: 10.1002/adma.201806692.

- [13] X. Song, X. Ji, M. Li, W. Lin, X. Luo, and H. Zhang, "A review on development prospect of CZTS based thin film solar cells," *International Journal of Photoenergy*, vol. 2014. Hindawi Publishing Corporation, 2014, doi: 10.1155/2014/613173.
- [14] T. Zdanowicz, T. Rodziewicz, and M. Zabkowska-Waclawek, "Theoretical analysis of the optimum energy band gap of semiconductors for fabrication of solar cells for applications in higher latitudes locations," in *Solar Energy Materials and Solar Cells*, 2005, vol. 87, no. 1-4, pp. 757-769, doi: 10.1016/j.solmat.2004.07.049.
- [15] M. Ravindiran and C. Praveenkumar, "Status review and the future prospects of CZTS based solar cell – A novel approach on the device structure and material modeling for CZTS based photovoltaic device," *Renewable and Sustainable Energy Reviews*, vol. 94. Elsevier Ltd, pp. 317-329, 01-Oct-2018, doi: 10.1016/j.rser.2018.06.008.
- [16] P. Prabeesh, P. Saritha, I. P. Selvam, and S. N. Potty, "Fabrication of CZTS thin films by dip coating technique for solar cell applications," *Materials Research Bulletin*, vol. 86, pp. 295-301, Feb. 2017, doi: 10.1016/j.materresbull.2016.10.033.
- [17] C. J. Bosson, M. T. Birch, D. P. Halliday, K. S. Knight, A. S. Gibbs, and P. D. Hatton, "Cation disorder and phase transitions in the structurally complex solar cell material $\text{Cu}_2\text{ZnSnS}_4$," *Journal of Materials Chemistry A*, vol. 5, no. 32, pp. 16672-16680, Aug. 2017, doi: 10.1039/c7ta03603e.
- [18] M. Ravindiran and C. Praveenkumar, "Status review and the future prospects of CZTS based solar cell – A novel approach on the device structure and material modeling for CZTS based photovoltaic device," *Renewable and Sustainable Energy Reviews*, vol. 94. Elsevier Ltd, pp. 317-329, 01-Oct-2018, doi: 10.1016/j.rser.2018.06.008.
- [19] S. A. Vanalakar *et al.*, "A review on pulsed laser deposited CZTS thin films for solar cell applications," *Journal of Alloys and Compounds*, vol. 619. Elsevier Ltd, pp. 109-121, 15-Jan-2015, doi: 10.1016/j.jallcom.2014.09.018.
- [20] Z. O. Elhmaidi, R. Pandiyan, M. Abd-Lefdil, and M. A. el Khakani, "Pulsed laser deposition of CZTS thin films, their thermal annealing and integration into n-Si/CZTS photovoltaic devices," in *Proceedings of 2016 International Renewable and Sustainable Energy Conference, IRSEC 2016*, 2017, pp. 130-135, doi: 10.1109/IRSEC.2016.7983988.
- [21] C. Yan *et al.*, "Boosting the efficiency of pure sulfide CZTS solar cells using the In/Cd-based hybrid buffers," *Solar Energy Materials and Solar Cells*, vol. 144, pp. 700-706, Jan. 2016, doi: 10.1016/j.solmat.2015.10.019.
- [22] Y. Feng *et al.*, "Searching for a fabrication route of efficient $\text{Cu}_2\text{ZnSnS}_4$ solar cells by post-sulfuration of co-sputtered Sn-enriched precursors," *Journal of Materials Chemistry C*, vol. 3, no. 37, pp. 9650-9656, Aug. 2015, doi: 10.1039/c5tc02486b.
- [23] R. Nakamura, K. Tanaka, H. Uchiki, K. Jimbo, T. Washio, and H. Katagiri, " $\text{Cu}_2\text{ZnSnS}_4$ thin film deposited by sputtering with $\text{Cu}_2\text{ZnSnS}_4$ compound target," *Japanese Journal of Applied Physics*, vol. 53, no. 2 PART 2, p. 02BC10, Jan. 2014, doi: 10.7567/JJAP.53.02BC10.

- [24] Y. Li, J. Chen, and J. Ma, "Properties of Cu₂ZnSnS₄ (CZTS) thin films prepared by plasma assisted co-evaporation," *Journal of Materials Science: Materials in Electronics*, vol. 26, no. 9, pp. 6546–6551, Sep. 2015, doi: 10.1007/s10854-015-3251-5.
- [25] A. Kumar, P. Ranjan, and A. D. Thakur, "Secondary Phases in CZTS Thin Films Grown Using Direct Liquid Coating Approach," in *Materials Today: Proceedings*, 2018, vol. 5, no. 1, pp. 99–103, doi: 10.1016/j.matpr.2017.11.059.
- [26] S. M. Pawar *et al.*, "Single step electrosynthesis of Cu₂ZnSnS₄ (CZTS) thin films for solar cell application," *Electrochimica Acta*, vol. 55, no. 12, pp. 4057–4061, Apr. 2010, doi: 10.1016/j.electacta.2010.02.051.
- [27] U. Syafiq, N. Ataollahi, R. DiMaggio, and P. Scardi, "Solution-based synthesis and characterization of Cu₂ZnSnS₄ (CZTS) thin films," *Molecules*, vol. 24, no. 19, Sep. 2019, doi: 10.3390/molecules24193454.
- [28] S. A. Vanalakar *et al.*, "A review on pulsed laser deposited CZTS thin films for solar cell applications," *Journal of Alloys and Compounds*, vol. 619. Elsevier Ltd, pp. 109–121, 15-Jan-2015, doi: 10.1016/j.jallcom.2014.09.018.
- [29] A. Nagoya, R. Asahi, R. Wahl, and G. Kresse, "Defect formation and phase stability of Cu₂ZnSnS₄ photovoltaic material," *Physical Review B - Condensed Matter and Materials Physics*, vol. 81, no. 11, p. 113202, Mar. 2010, doi: 10.1103/PhysRevB.81.113202.
- [30] M. Kumar, A. Dubey, N. Adhikari, S. Venkatesan, and Q. Qiao, "Strategic review of secondary phases, defects and defect-complexes in kesterite CZTS-Se solar cells," *Energy and Environmental Science*, vol. 8, no. 11, pp. 3134–3159, Nov. 2015, doi: 10.1039/c5ee02153g.
- [31] K. Pal, P. Singh, A. Bhaduri, and K. B. Thapa, "Current challenges and future prospects for a highly efficient (>20%) kesterite CZTS solar cell: A review," *Solar Energy Materials and Solar Cells*, vol. 196, pp. 138–156, Jul. 2019, doi: 10.1016/j.solmat.2019.03.001.
- [32] M. A. Green *et al.*, "Solar cell efficiency tables (Version 53)," *Progress in Photovoltaics: Research and Applications*, vol. 27, no. 1, pp. 3–12, Jan. 2019, doi: 10.1002/pip.3102.
- [33] S. H. Hadke *et al.*, "Synergistic Effects of Double Cation Substitution in Solution-Processed CZTS Solar Cells with over 10% Efficiency," *Advanced Energy Materials*, vol. 8, no. 32, p. 1802540, Nov. 2018, doi: 10.1002/aenm.201802540.
- [34] A. Guchhait *et al.*, "Enhancement of Open-Circuit Voltage of Solution-Processed Cu₂ZnSnS₄ Solar Cells with 7.2% Efficiency by Incorporation of Silver," *ACS Energy Letters*, vol. 1, no. 6, pp. 1256–1261, Dec. 2016, doi: 10.1021/acsenergylett.6b00509.
- [35] S. Chen, A. Walsh, X.-G. Gong, and S.-H. Wei, "Classification of Lattice Defects in the Kesterite Cu₂ZnSnS₄ and Cu₂ZnSnSe₄ Earth-Abundant Solar Cell Absorbers," *Advanced Materials*, vol. 25, no. 11, pp. 1522–1539, Mar. 2013, doi: 10.1002/adma.201203146.
- [36] Y. E. Romanyuk *et al.*, "Doping and alloying of kesterites," *Journal of Physics: Energy*, vol. 1, no. 4, p. 044004, Aug. 2019, doi: 10.1088/2515-7655/AB23BC.

- [37] T. Gershon *et al.*, "Photovoltaic Materials and Devices Based on the Alloyed Kesterite Absorber ($\text{Ag}_x\text{Cu}_{1-x}$)₂ZnSnSe₄," *Advanced Energy Materials*, vol. 6, no. 10, p. 1502468, May 2016, doi: 10.1002/aenm.201502468.
- [38] Z.-K. Yuan *et al.*, "Engineering Solar Cell Absorbers by Exploring the Band Alignment and Defect Disparity: The Case of Cu- and Ag-Based Kesterite Compounds," *Advanced Functional Materials*, vol. 25, no. 43, pp. 6733–6743, Nov. 2015, doi: 10.1002/adfm.201502272.
- [39] P. K. Sarswat and M. L. Free, "The effects of dopant impurities on Cu₂ZnSnS₄ system Raman properties," *Journal of Materials Science*, vol. 50, no. 4, pp. 1613–1623, Nov. 2015, doi: 10.1007/s10853-014-8722-1.
- [40] S. G. Haass *et al.*, "Complex Interplay between Absorber Composition and Alkali Doping in High-Efficiency Kesterite Solar Cells," *Advanced Energy Materials*, vol. 8, no. 4, p. 1701760, Feb. 2018, doi: 10.1002/aenm.201701760.
- [41] T. Abzieher, T. Schnabel, M. Hetterich, M. Powalla, and E. Ahlswede, "Source and effects of sodium in solution-processed kesterite solar cells," *physica status solidi (a)*, vol. 213, no. 4, pp. 1039–1049, Apr. 2016, doi: 10.1002/pssa.201532619.
- [42] A. Cabas-Vidani *et al.*, "High-Efficiency ($\text{Li}_x\text{Cu}_{1-x}$)₂ZnSn(S,Se)₄ Kesterite Solar Cells with Lithium Alloying," *Advanced Energy Materials*, vol. 8, no. 34, p. 1801191, Dec. 2018, doi: 10.1002/aenm.201801191.
- [43] T. Maeda, A. Kawabata, and T. Wada, "First-principles study on alkali-metal effect of Li, Na, and K in Cu₂ZnSnS₄ and Cu₂ZnSnSe₄," *physica status solidi (c)*, vol. 12, no. 6, pp. 631–637, Jun. 2015, doi: 10.1002/pssc.201400345.
- [44] W. Li *et al.*, "Revealing the Role of Potassium Treatment in CZTSSe Thin Film Solar Cells," 2017, doi: 10.1021/acs.chemmater.7b00418.
- [45] Y.-T. Hsieh *et al.*, "Efficiency Enhancement of Cu₂ZnSn(S,Se)₄ Solar Cells via Alkali Metals Doping," *Advanced Energy Materials*, vol. 6, no. 7, p. 1502386, Apr. 2016, doi: 10.1002/aenm.201502386.
- [46] R. Caballero *et al.*, "Effect of Magnesium Incorporation on Solution-Processed Kesterite Solar Cells," *Frontiers in Chemistry*, vol. 6, no. JAN, p. 5, Jan. 2018, doi: 10.3389/fchem.2018.00005.
- [47] S. Kim, K. M. Kim, H. Tampo, H. Shibata, K. Matsubara, and S. Niki, "Ge-incorporated Cu₂ZnSnSe₄ thin-film solar cells with efficiency greater than 10%," *Solar Energy Materials and Solar Cells*, vol. 144, pp. 488–492, Jan. 2016, doi: 10.1016/j.solmat.2015.09.039.
- [48] S. Kim, K. M. Kim, H. Tampo, H. Shibata, and S. Niki, "Improvement of voltage deficit of Ge-incorporated kesterite solar cell with 12.3% conversion efficiency," *Applied Physics Express*, vol. 9, no. 10, p. 102301, Oct. 2016, doi: 10.7567/APEX.9.102301.
- [49] S. Lie *et al.*, "Improving the charge separation and collection at the buffer/absorber interface by double-layered Mn-substituted CZTS," *Solar Energy Materials and Solar Cells*, vol. 185, pp. 351–358, Oct. 2018, doi: 10.1016/j.solmat.2018.05.052.

- [50] X. Li *et al.*, "Efficient Optimization of the Performance of Mn²⁺-Doped Kesterite Solar Cell: Machine Learning Aided Synthesis of High Efficient Cu₂(Mn,Zn)Sn(S,Se)₄ Solar Cells," *Solar RRL*, vol. 2, no. 12, Dec. 2018, doi: 10.1002/SOLR.201800198.
- [51] S. H. Hadke *et al.*, "Synergistic Effects of Double Cation Substitution in Solution-Processed CZTS Solar Cells with over 10% Efficiency," *Advanced Energy Materials*, vol. 8, no. 32, p. 1802540, Nov. 2018, doi: 10.1002/aenm.201802540.
- [52] J. Li, D. Wang, X. Li, Y. Zeng, and Y. Zhang, "Cation Substitution in Earth-Abundant Kesterite Photovoltaic Materials," *Advanced Science*, vol. 5, no. 4, p. 1700744, Apr. 2018, doi: 10.1002/advs.201700744.
- [53] H. Cui, C.-Y. Lee, W. Li, X. Liu, X. Wen, and X. Hao, "Improving Efficiency of Evaporated Cu₂ZnSnS₄ Thin Film Solar Cells by a Thin Ag Intermediate Layer between Absorber and Back Contact," 2015, doi: 10.1155/2015/170507.
- [54] G. Sai Gautam, T. P. Senftle, and E. A. Carter, "Understanding the Effects of Cd and Ag Doping in Cu₂ZnSnS₄ Solar Cells," *Chemistry of Materials*, vol. 30, no. 14, pp. 4543–4555, Jul. 2018, doi: 10.1021/acs.chemmater.8b00677.
- [55] Z. Su, J. M. R. Tan, X. Li, X. Zeng, S. K. Batabyal, and L. H. Wong, "Cation Substitution of Solution-Processed Cu₂ZnSnS₄ Thin Film Solar Cell with over 9% Efficiency," *Advanced Energy Materials*, vol. 5, no. 19, p. 1500682, Oct. 2015, doi: 10.1002/aenm.201500682.
- [56] S. G. Haass, "Alkali Treatment of Solution Processed Kesterite Solar Cells," 2017, doi: 10.3929/ETHZ-B-000235925.
- [57] Y. Qi *et al.*, "Elemental Precursor Solution Processed (Cu_{1-x}Ag_x)₂ZnSn(S,Se)₄ Photovoltaic Devices with over 10% Efficiency," 2017, doi: 10.1021/ACSAMI.7B03944.
- [58] K. Timmo *et al.*, "Sulfur-containing Cu₂ZnSnSe₄ monograin powders for solar cells," *Solar Energy Materials and Solar Cells*, vol. 94, no. 11, pp. 1889–1892, Nov. 2010, doi: 10.1016/j.solmat.2010.06.046.
- [59] M. Altosaar *et al.*, "Further developments in CIS monograin layer solar cells technology," in *Solar Energy Materials and Solar Cells*, 2005, vol. 87, no. 1–4, pp. 25–32, doi: 10.1016/j.solmat.2004.09.021.
- [60] E. Mellikov *et al.*, "Growth of CZTS-Based Monograins and Their Application to Membrane Solar Cells," in *Copper Zinc Tin Sulfide-Based Thin-Film Solar Cells*, Wiley, 2015, pp. 289–309.
- [61] "(PDF) CZTS (Cu₂ZnSnSe₄) CRYSTAL GROWTH FOR USE IN MONOGRAIN MEMBRANE SOLAR CELLS." [Online]. Available: https://www.researchgate.net/publication/284715065_CZTS_Cu_2_ZnSnSe_4_CRYSTAL_GROWTH_FOR_USE_IN_MONOGRAIN_MEMBRANE_SOLAR_CELLS. [Accessed: 25-Feb-2020].
- [62] M. Danilson, "Temperature Dependent Electrical Properties of Kesterite Monograin Layer Solar Cells," Ph.D. dissertation, Tallinn University of Technology, Estonia, 2016.
- [63] "Renewables 2019 – Analysis – IEA." [Online]. Available: <https://www.iea.org/reports/renewables-2019>. [Accessed: 26-Mar-2020].

- [64] "Study of Cu₂(Zn,Cd)SnS₄ absorber materials for monograin layer solar cells = Päikesepatareides kasutatavate Cu₂(Zn,Cd)SnS₄ absorbermaterjalide uurimine | Digar viewer." [Online]. Available: <https://www.digar.ee/viewer/et/nlib-digar:326266/285667/page/2>. [Accessed: 14-Apr-2020].
- [65] R. S. Das and Y. K. Agrawal, "Raman spectroscopy: Recent advancements, techniques and applications," *Vibrational Spectroscopy*, vol. 57, no. 2. Elsevier, pp. 163–176, 01-Nov-2011, doi: 10.1016/j.vibspec.2011.08.003.
- [66] I. Leinemann *et al.*, "Reaction pathway to Cu₂ZnSnSe₄ formation in CdI₂: Part 1. Chemical reactions and enthalpies in mixtures of CdI₂–ZnSe, CdI₂–SnSe, and CdI₂–CuSe," *Journal of Thermal Analysis and Calorimetry*, vol. 134, no. 1, pp. 409–421, Oct. 2018, doi: 10.1007/s10973-018-7102-5.
- [67] K. Timmo *et al.*, "Comparative study of SnS recrystallization in molten CdI₂, SnCl₂ and KI," *physica status solidi (c)*, vol. 13, no. 1, pp. 8–12, Jan. 2016, doi: 10.1002/pssc.201510082.
- [68] K. S. Gour, O. P. Singh, J. S. Tawale, and V. N. Singh, "Silver (Ag) incorporated Cu₂ZnSnS₄ thin film for improved optical and morphological properties," *Superlattices and Microstructures*, vol. 120, pp. 54–59, Aug. 2018, doi: 10.1016/j.spmi.2018.05.012.
- [69] W. C. Huang, S. Y. Wei, C. H. Cai, W. H. Ho, and C. H. Lai, "The role of Ag in aqueous solution processed (Ag,Cu)₂ZnSn(S,Se)₄ kesterite solar cells: Antisite defect elimination and importance of Na passivation," *Journal of Materials Chemistry A*, vol. 6, no. 31, pp. 15170–15181, Aug. 2018, doi: 10.1039/c8ta02950d.
- [70] B. Zhou, D. Xia, and Y. Wang, "Phase-selective synthesis and formation mechanism of CZTS nanocrystals," *RSC Advances*, vol. 5, no. 86, pp. 70117–70126, Aug. 2015, doi: 10.1039/c5ra11890e.
- [71] M. Guc *et al.*, "Polarized Raman scattering study of kesterite type Cu₂ZnSnS₄ single crystals," *Scientific Reports*, vol. 6, no. 1, pp. 1–7, Jan. 2016, doi: 10.1038/srep19414.
- [72] M. Dimitrievska *et al.*, "Multiwavelength excitation Raman scattering study of polycrystalline kesterite Cu₂ZnSnS₄ thin films," *Applied Physics Letters*, vol. 104, no. 2, p. 021901, Jan. 2014, doi: 10.1063/1.4861593.
- [73] J. Fu *et al.*, "Improving the Performance of Solution-Processed Cu₂ZnSn(S,Se)₄ Photovoltaic Materials by Cd²⁺ Substitution," *Chemistry of Materials*, vol. 28, no. 16, pp. 5821–5828, Aug. 2016, doi: 10.1021/acs.chemmater.6b02111.
- [74] J. Krustok, R. Josepson, T. Raadik, and M. Danilson, "Potential fluctuations in Cu₂ZnSnSe₄ solar cells studied by temperature dependence of quantum efficiency curves," *Physica B: Condensed Matter*, vol. 405, no. 15, pp. 3186–3189, Aug. 2010, doi: 10.1016/j.physb.2010.04.041.